

Raman heterodyne detection of nuclear magnetic resonance

N. C. Wong, E. S. Kintzer, J. Mlynek,* R. G. DeVoe, and R. G. Brewer
*IBM Research Laboratory, San Jose, California 95193 and Department of Applied Physics,
 Stanford University, Stanford, California 94305*

(Received 13 June 1983)

A novel coherent Raman effect induced by a laser and a radio-frequency (rf) field is used to detect cw and pulsed nuclear magnetic resonance (NMR) in ground and excited electronic states. The effect is illustrated in the impurity-ion solid $\text{Pr}^{3+}:\text{LaF}_3$ at 1.6 K utilizing the Pr^{3+} optical transition ${}^3H_4(\Gamma_1) \rightarrow {}^1D_2(\Gamma_1)$. The laser field of frequency ω_E and the rf field (ω_H) induce a light wave at the sum $\omega_E + \omega_H$ (anti-Stokes) and difference $\omega_E - \omega_H$ (Stokes) frequencies, generating an absorptive or dispersive heterodyne beat signal (ω_H) with the laser field at a photodetector. The theory of this effect is characterized in a new three-level perturbation calculation which requires, unlike the usual stimulated Raman effect, that all three transitions be electric- or magnetic-dipole allowed. Detailed predictions are confirmed by cw measurements of the $\text{Pr}^{3+}:\text{LaF}_3$ hyperfine splittings where the optical heterodyne signals are shot-noise limited. The Pr^{3+} nuclear quadrupole parameters are obtained for the 3H_4 and 1D_2 states where the line centers are determined with kilohertz precision. The corresponding wave functions show significant hyperfine-state mixing, as required for all three transitions to be dipole allowed. The cw line shapes are narrow (30–160 kHz), inhomogeneously broadened by nuclear magnetic interactions, and reveal either a Gaussian or an anomalous second-derivative-like line shape. The spin-echo measurements for the 3H_4 and 1D_2 hyperfine transitions yield homogeneous line shapes which are Lorentzian, and rather surprisingly, linewidths in the narrow range 10–20 kHz, a result which tests current line-broadening theories.

I. INTRODUCTION

Recently we reported a preliminary account of Raman heterodyne detection,¹ a new way of observing nuclear magnetic resonance (NMR). The purpose of this paper is to relate a number of the details of this technique, its theory, its advantages, and some applications. This method, which utilizes a coherent optical and radio-frequency (rf) induced Raman effect, is capable of monitoring coherent spin transients or nuclear resonances under cw conditions in both ground and optically excited states with high sensitivity and precision. Dilute systems in the gas phase or solid state which are inaccessible by conventional NMR can now be examined. The method, which surpasses previous rf-optical techniques,^{2–4} has been demonstrated in a dilute rare-earth impurity-ion crystal $\text{Pr}^{3+}:\text{LaF}_3$, where the first spin-echo measurements of an electronic excited state are made, and cw resonances yield NMR line centers and shapes with kilohertz precision. Here we report further measurements which allow us to compare for the first time NMR and optical dephasing studies^{5–8} and to test current line-broadening theory.⁹

In Fig. 1, the $\text{Pr}^{3+}(I = \frac{5}{2})$ hyperfine-energy-level diagram reveals the basic stimulated Raman effect where an optical field at the frequency ω_E (solid arrow) and an rf field at the frequency ω_H (wavy arrow) drive two coupled transitions resonantly, which combine in a two-photon process to generate a coherent anti-Stokes field at the sum frequency $\omega'_E = \omega_E + \omega_H$. In addition, a Stokes field at the difference frequency $\omega_E - \omega_H$, due to a second resonant packet, accompanies the above anti-Stokes field. In Fig. 2,

the two optical fields ω_E and ω'_E produce at the photodetector a heterodyne beat signal of frequency $\omega_H = |\omega_E - \omega'_E|$. This optical heterodyne process enhances detection sensitivity and is closely related to that used in Stark- or laser-frequency switching experiments.¹⁰

Unlike the usual stimulated Raman effect,¹¹ this is a resonant process in which all three transitions are either electric or magnetic dipole allowed. The technique can be generalized to any three-level systems where all three tran-

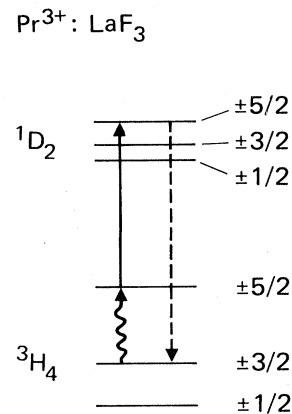


FIG. 1. Hyperfine energy level diagram for the 5925-Å 3H_4 - 1D_2 transition of $\text{Pr}^{3+}:\text{LaF}_3$, showing the coherent Raman process. The wavy arrow indicates the rf driving field, while the solid arrow represents the optical driving field. The coherently generated anti-Stokes field is shown as a dashed line.

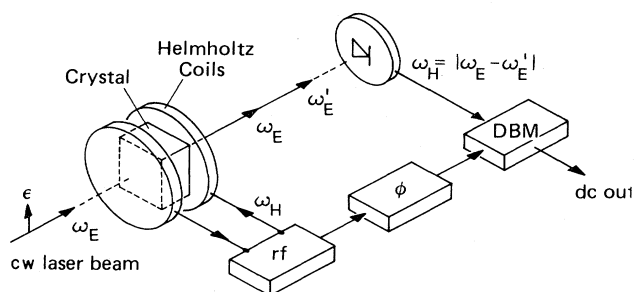


FIG. 2. Simplified schematic of the experimental arrangement for Raman heterodyne detection of cw or pulsed NMR.

sitions are active, allowing sensitive detections of NMR, electron spin resonance (ESR), or even infrared transitions. In addition to $\text{Pr}^{3+}:\text{LaF}_3$, similar measurements have been performed on $\text{Pr}^{3+}:\text{YAlO}_3$ (Ref. 12), samarium vapor,¹³ and sodium vapor.

Our work thus extends previous coherent techniques as in optical-pumping double resonance,¹⁴ coherent optical double resonance,¹⁵ coherent Raman beats,¹⁶ photon-echo modulation,¹⁷ photon-echo nuclear double resonance,⁴ and Raman echoes,^{18,19} or those methods which rely on incoherent detection as in enhanced and saturated absorption²⁰ and rf-optical double resonance.^{2,3}

There is currently considerable interest in the impurity-ion solid $\text{Pr}^{3+}:\text{LaF}_3$. Optical dephasing (relaxation time T_2) measurements on the $^1D_2 \leftrightarrow ^3H_4$ transition have been carried out with the use of different laser techniques⁵⁻⁷ and very narrow optical homogeneous linewidths of a few kilohertz have been obtained. The dominant optical line-broadening mechanism has been determined to be the $^{19}\text{F}-^{19}\text{F}$ dipolar interaction, where spin-flip fluctuations of the ^{19}F nuclei impress weak fluctuating magnetic fields on the ^{141}Pr nuclei and perturb the Pr^{3+} optical transition frequency through the Pr-F nuclear dipole-dipole interaction. This has been confirmed by a Monte Carlo calculation⁹ and by magic-angle line-narrowing experiments.^{5,7} In addition a recent experiment⁸ shows that at high laser intensities the system $\text{Pr}^{3+}:\text{LaF}_3$ is no longer adequately described by the optical Bloch equations²¹ and exhibits a Redfield-type saturation behavior²² in the optical T_2 . A full understanding of these measurements requires establishing a link between the optical dephasing measurements and the NMR line-broadening mechanisms of each hyperfine transition, a task that can be accomplished by the present technique.

II. THEORY

In this section we present a new theory for the interaction of two resonant electromagnetic fields with a three-level system using a density-matrix perturbation method. Our theory differs from previous three-level calculations^{11,18,23} involving Raman scattering or two-photon transitions in that we assume all three transitions are dipole allowed. This introduces additional terms in the equations of motion with new solutions. This assumption

is satisfied in the $\text{Pr}^{3+}:\text{LaF}_3$ $^1D_2 \leftrightarrow ^3H_4$ transition because of hyperfine state mixing in the 1D_2 excited state. In lowest order our theory predicts a three-wave mixing effect while the usual stimulated Raman scattering and two-photon transitions are four-wave mixing processes.¹¹ When the condition of a weak rf excitation is relaxed, we show that both linear and nonlinear processes of the NMR transition can be optically monitored.

A. Equations of motion

In Fig. 3, the energy-level diagram shows that the Raman levels 1 and 2 are closely lying states whose energy separation may be radio frequency as in NMR, microwave as in ESR, or infrared as in molecular ro-vibrational levels, and level 3 is separated from them by a much larger energy in the optical-frequency range. Level 3 may lie higher than the Raman levels, as shown in Fig. 3, or lower such that the Raman levels may be hyperfine states of an electronic ground or excited state.

A laser field

$$\vec{E}_0(z,t) = \frac{1}{2} E_0 e^{i(\omega_E t - k_E z)} \hat{e}_1 + \text{c.c.} \quad (2.1a)$$

connects level 3 optically to the Raman levels, which are coupled by an rf magnetic field

$$\vec{H}_1(t) = \frac{1}{2} H_1 e^{i\omega_H t} \hat{e}_2 + \text{c.c.} \quad (2.1b)$$

Although we assume \vec{H}_1 is a magnetic field, our formulation is applicable for any electromagnetic wave. The frequencies of \vec{E}_0 and \vec{H}_1 are assumed to satisfy the condition

$$\omega_E \gg \omega_H. \quad (2.2)$$

In Eq. (2.1b) the spatial dependence of \vec{H}_1 is ignored because the wavelength of \vec{H}_1 is much larger than the interaction region.

The density-matrix equations of motion are given, with neglect of damping terms (represented by the ellipsis), by

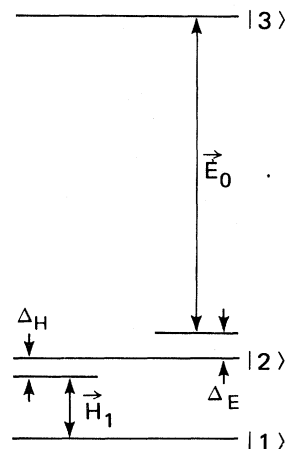


FIG. 3. Energy-level diagram for the stimulated Raman process in a three-level atom. \vec{H}_1 excites the $1 \rightarrow 2$ rf transition and \vec{E}_0 excites the $2 \rightarrow 3$ optical transition.

$$i\hbar \frac{\partial \rho}{\partial t} = [\mathcal{H}, \rho] + \dots, \quad (2.3)$$

where the Hamiltonian $\mathcal{H} = \mathcal{H}_0 + \mathcal{H}'$ consists of the field-free Hamiltonian \mathcal{H}_0 and the dipole interactions

$$\mathcal{H}' = -\vec{\mu}_E \cdot \vec{E}_0 - \vec{\mu}_H \cdot \vec{H}_1$$

satisfying the usual conditions

$$\langle i | \mathcal{H}_0 | j \rangle = \hbar \omega_i \delta_{ij},$$

$$\langle i | \mathcal{H}' | i \rangle = 0, \quad i, j = 1, 2, 3.$$

Here $\vec{\mu}_E$ and $\vec{\mu}_H$ are the electric and magnetic dipole moment operators, respectively. The dipole coupling strengths are given by the parameters

$$\alpha_1 \equiv \frac{E_0}{2\hbar} \langle 1 | \vec{\mu}_E \cdot \hat{e}_1 | 3 \rangle \equiv \frac{E_0 \mu_{13}}{2\hbar}, \quad (2.4a)$$

$$\alpha_2 \equiv \frac{E_0}{2\hbar} \langle 2 | \vec{\mu}_E \cdot \hat{e}_1 | 3 \rangle \equiv \frac{E_0 \mu_{23}}{2\hbar}, \quad (2.4b)$$

$$\beta \equiv \frac{H_1}{2\hbar} \langle 1 | \vec{\mu}_H \cdot \hat{e}_2 | 2 \rangle \equiv \frac{H_1 \mu_{12}}{2\hbar}, \quad (2.4c)$$

and μ_{ij} is assumed real. The parameters are related to the Rabi frequency by

$$\alpha_1 = \frac{1}{2} \chi_1, \quad \alpha_2 = \frac{1}{2} \chi_2, \quad \beta = \frac{1}{2} \chi. \quad (2.5)$$

For an optically thin sample, the optical signal field

$$\vec{E}_s(z, t) = \vec{E}_s(z, t) e^{i(\omega_E t - k_E z)} \hat{e}_1 + \text{c.c.} \quad (2.6)$$

obeys Maxwell's wave equation

$$\frac{\partial \vec{E}_s}{\partial z} = -2\pi i k_E \langle \vec{P}_s \rangle, \quad (2.7)$$

where the tilde denotes the slowly varying part. The Raman signal polarization

$$\langle \vec{P}_s(t) \rangle = N (\mu_{31} \langle \tilde{\rho}_{13}(t) \rangle + \mu_{32} \langle \tilde{\rho}_{23}(t) \rangle) \quad (2.8)$$

is to be averaged over the crystal strain and magnetic inhomogeneous line shapes which are assumed Gaussian. The angular brackets in (2.7) and (2.8) denote this average, and N is the number density.

The signal field \vec{E}_s (2.6) and the input laser field \vec{E}_0 (2.1a) give rise to the total field

$$\begin{aligned} \vec{E}_T &= \vec{E}_0 + \vec{E}_s \\ &= \vec{E}_T e^{i(\omega_E t - k_E z)} \hat{e}_1 + \text{c.c.}, \end{aligned} \quad (2.9a)$$

where

$$\vec{E}_T = \frac{1}{2} E_0 + \vec{E}_s. \quad (2.9b)$$

From the total intensity $I_T = E_T E_T^*$, one obtains the observable heterodyne beat signal

$$I_s = \frac{1}{2} \vec{E}_s E_0^* + \text{c.c.} \quad (2.10)$$

We introduce phenomenologically the population decay rates γ_i for state $|i\rangle$, and the transverse decay rates $\gamma_{ij} = \gamma_{ji}$ between states $|i\rangle$ and $|j\rangle$. By defining

$$\rho_{12}(t) = \tilde{\rho}_{12} e^{i\omega_H t}, \quad (2.11a)$$

$$\rho_{13}(z, t) = \tilde{\rho}_{13}(t) e^{i(\omega_E t - k_E z)}, \quad (2.11b)$$

$$\rho_{23}(z, t) = \tilde{\rho}_{23}(t) e^{i(\omega_E t - k_E z)}, \quad (2.11c)$$

and applying the rotating-wave approximation (RWA) which neglects the nonresonant terms, the equations of motion (2.3) become

$$\dot{\rho}_{11} = -\gamma_1 (\rho_{11} - \rho_{11}^0) + (i\beta \tilde{\rho}_{21} + i\alpha_1 \tilde{\rho}_{31} + \text{c.c.}), \quad (2.12a)$$

$$\dot{\rho}_{22} = -\gamma_2 (\rho_{22} - \rho_{22}^0) + (i\beta^* \tilde{\rho}_{12} + i\alpha_2 \tilde{\rho}_{32} + \text{c.c.}), \quad (2.12b)$$

$$\dot{\rho}_{33} = -\gamma_3 (\rho_{33} - \rho_{33}^0) + (i\alpha_1^* \tilde{\rho}_{13} + i\alpha_2^* \tilde{\rho}_{23} + \text{c.c.}), \quad (2.12c)$$

$$\begin{aligned} \dot{\tilde{\rho}}_{12} &= (i\Delta_H - \gamma_{12}) \tilde{\rho}_{12} + i\beta (\rho_{22} - \rho_{11}) \\ &\quad + (i\alpha_1 \tilde{\rho}_{32} - i\alpha_2^* \tilde{\rho}_{13}) e^{-i\omega_H t}, \end{aligned} \quad (2.12d)$$

$$\begin{aligned} \dot{\tilde{\rho}}_{13} &= [i(\Delta_E + \omega_{21}) - \gamma_{13}] \tilde{\rho}_{13} + i\alpha_1 (\rho_{33} - \rho_{11}) \\ &\quad - i\alpha_2 \tilde{\rho}_{12} e^{i\omega_H t} + i(\beta e^{i\omega_H t} + \text{c.c.}) \tilde{\rho}_{23}, \end{aligned} \quad (2.12e)$$

$$\begin{aligned} \dot{\tilde{\rho}}_{23} &= (i\Delta_E - \gamma_{23}) \tilde{\rho}_{23} + i\alpha_2 (\rho_{33} - \rho_{22}) \\ &\quad - i\alpha_1 \tilde{\rho}_{21} e^{-i\omega_H t} + i(\beta e^{i\omega_H t} + \text{c.c.}) \tilde{\rho}_{13}. \end{aligned} \quad (2.12f)$$

Here the tuning parameters Δ_H and Δ_E are defined by

$$\Delta_H \equiv \omega_{21} - \omega_H, \quad \Delta_E \equiv \omega_{32} - \omega_E, \quad (2.12g)$$

and $\omega_{ij} \equiv \omega_i - \omega_j$ is the frequency separation between states $|i\rangle$ and $|j\rangle$. ρ_{ii}^0 is the field-free population for state $|i\rangle$ at thermal equilibrium.

The RWA assumes that $\tilde{\rho}_{ij}(t)$ is slowly varying with respect to the corresponding frequency $|\omega_{ij}|$. This implies that $\tilde{\rho}_{13}(t)$ and $\tilde{\rho}_{23}(t)$ are allowed to have components which vary at the rate ω_H since we have assumed $\omega_E \gg \omega_H$ (2.2). Despite the presence of $e^{-i\omega_H t}$ in Eq. (2.12d),²⁴ the primary signal of ρ_{12} (2.18b) indeed satisfies the RWA assumption.

We should mention that in the equations of motion (2.12), optical-pumping effects are not taken into account partly because of the complexity in modeling them, but also because they occur on a much longer time scale than that of the experiment. Although optical pumping can significantly affect the population levels ρ_{ii}^0 , we show in Sec. V A that even when the time scale of the experiment approaches that of optical pumping, the essential features remain unchanged.

B. Perturbation solution

Within the RWA we seek a perturbative stationary solution to the equations of motion (2.12) by assuming that the excitation fields \vec{E}_0 and \vec{H}_1 are weak. In Sec. II E, we relax the weak-field condition on \vec{H}_1 to obtain a more general time-dependent solution. Formally integrating Eqs. (2.12), we obtain

$$\rho_{11}(t) = \rho_{11}^0 + \int_0^t dt' e^{-\gamma_1(t-t')} [i\beta\tilde{\rho}_{21}(t') + i\alpha_1\tilde{\rho}_{31}(t') + \text{c.c.}], \quad (2.13a)$$

$$\rho_{22}(t) = \rho_{22}^0 + \int_0^t dt' e^{-\gamma_2(t-t')} [i\beta^*\tilde{\rho}_{12}(t') + i\alpha_2\tilde{\rho}_{32}(t') + \text{c.c.}], \quad (2.13b)$$

$$\rho_{33}(t) = \rho_{33}^0 + \int_0^t dt' e^{-\gamma_3(t-t')} [i\alpha_1^*\tilde{\rho}_{13}(t') + i\alpha_2^*\tilde{\rho}_{23}(t') + \text{c.c.}], \quad (2.13c)$$

$$\tilde{\rho}_{12}(t) = \int_0^t dt' e^{(i\Delta_H - \gamma_{12})(t-t')} \{i\beta[\rho_{22}(t') - \rho_{11}(t')] + [i\alpha_1\tilde{\rho}_{32}(t') - i\alpha_2^*\tilde{\rho}_{13}(t')]e^{-i\omega_H t'}\}, \quad (2.13d)$$

$$\tilde{\rho}_{13}(t) = \int_0^t dt' e^{[(i\Delta_E + \omega_{21}) - \gamma_{13}](t-t')} \{i\alpha_1[\rho_{33}(t') - \rho_{11}(t')] - i\alpha_2\tilde{\rho}_{12}(t')e^{i\omega_H t'} + i\tilde{\rho}_{23}(t')(\beta e^{i\omega_H t'} + \text{c.c.})\}, \quad (2.13e)$$

$$\tilde{\rho}_{23}(t) = \int_0^t dt' e^{(i\Delta_E - \gamma_{23})(t-t')} \{i\alpha_2[\rho_{33}(t') - \rho_{22}(t')] - i\alpha_1\tilde{\rho}_{21}(t')e^{-i\omega_H t'} + i\tilde{\rho}_{13}(t')(\beta e^{i\omega_H t'} + \text{c.c.})\}, \quad (2.13f)$$

with the initial conditions

$$\rho_{ii}(0) = \rho_{ii}^0 \quad (2.14)$$

and

$$\tilde{\rho}_{ij}(0) = 0, \quad i \neq j.$$

In the weak-field limit,

$$\alpha_1, \alpha_2, \beta \rightarrow 0, \quad (2.15)$$

we obtain a perturbative solution from the formal solution (2.13) in orders of α_1 , α_2 , and β , thus excluding power-broadening effects. We write

$$\tilde{\rho}_{ij} = \sum_n \tilde{\rho}_{ij}^{(n)}, \quad (2.16)$$

and

$$\rho_{ii} = \sum_n \rho_{ii}^{(n)},$$

where n denotes the order of perturbation. The zeroth-order field-free solution given by

$$\rho_{ii}^{(0)}(t) = \rho_{ii}^0, \quad i = 1, 2, 3, \quad (2.17a)$$

$$\tilde{\rho}_{ij}^{(0)}(t) = 0, \quad i \neq j, \quad (2.17b)$$

and the initial conditions (2.14) are used to obtain the first-order $n = 1$ solution

$$\rho_{ii}^{(1)}(t) = 0, \quad (2.18a)$$

$$\tilde{\rho}_{12}^{(1)}(t) = \frac{-i\beta(\rho_{22}^0 - \rho_{11}^0)}{i\Delta_H - \gamma_{12}} (1 - e^{(i\Delta_H - \gamma_{12})t}), \quad (2.18b)$$

$$\tilde{\rho}_{13}^{(1)}(t) = \frac{-i\alpha_1(\rho_{33}^0 - \rho_{11}^0)}{i(\Delta_E + \omega_{21}) - \gamma_{13}} (1 - e^{[i(\Delta_E + \omega_{21}) - \gamma_{13}]t}), \quad (2.18c)$$

$$\tilde{\rho}_{23}^{(1)}(t) = \frac{-i\alpha_2(\rho_{33}^0 - \rho_{22}^0)}{i\Delta_E - \gamma_{23}} (1 - e^{(i\Delta_E - \gamma_{23})t}). \quad (2.18d)$$

Substituting the first-order solution (2.18) into the formal solution (2.13), and letting $t \rightarrow \infty$ so that damping terms go to zero and only oscillatory terms remain, we obtain the stationary second-order $n = 2$ solution for $\tilde{\rho}_{13}$ and $\tilde{\rho}_{23}$:

$$\tilde{\rho}_{13}^{(2)}(t \rightarrow \infty) = \frac{\alpha_2\beta e^{i\omega_H t}}{i(\Delta_E + \Delta_H) - \gamma_{13}} \frac{\rho_{22}^0 - \rho_{11}^0}{i\Delta_H - \gamma_{12}} - \frac{\rho_{33}^0 - \rho_{22}^0}{i\Delta_E - \gamma_{23}} \left[\frac{\alpha_2\beta e^{i\omega_H t}}{i(\Delta_E + \Delta_H) - \gamma_{13}} + \frac{\alpha_2\beta^* e^{-i\omega_H t}}{i(\Delta_E + \omega_{21} + \omega_H) - \gamma_{13}} \right], \quad (2.19a)$$

$$\tilde{\rho}_{23}^{(2)}(t \rightarrow \infty) = \frac{\alpha_1\beta^* e^{-i\omega_H t}}{i(\Delta_E + \omega_H) - \gamma_{23}} \frac{\rho_{22}^0 - \rho_{11}^0}{i\Delta_H + \gamma_{12}} - \frac{\rho_{33}^0 - \rho_{11}^0}{i(\Delta_E + \omega_{21}) - \gamma_{13}} \left[\frac{\alpha_1\beta e^{i\omega_H t}}{i(\Delta_E - \omega_H) - \gamma_{23}} + \frac{\alpha_1\beta^* e^{-i\omega_H t}}{i(\Delta_E + \omega_H) - \gamma_{23}} \right]. \quad (2.19b)$$

The first-order solutions for $\tilde{\rho}_{13}$ and $\tilde{\rho}_{23}$ in (2.18c) and (2.18d) are proportional to E_0 , oscillate at the laser frequency ω_E in the laboratory frame, and reflect the forced oscillation of the dipoles due to the driving field \vec{E}_0 . The second-order solutions (2.19) are proportional to $E_0 |H_1|$, oscillate at $\omega_E \pm \omega_H$ in the laboratory frame, and reflect the two-quantum transitions.

The first term in the solutions (2.19a) and (2.19b) contributes to the Raman signal of the rf transition $1 \leftrightarrow 2$. This is also evident from the formal solution for $\tilde{\rho}_{13}$ (2.13e) and $\tilde{\rho}_{23}$ (2.13f), where the Raman signal, be it cw or transient, can only come from the terms $\alpha_2\tilde{\rho}_{12}$ in (2.13e) and $\alpha_1\tilde{\rho}_{21}$ in (2.13f).

The second term in (2.19a) and (2.19b) can be dropped because after it is averaged over the optical inhomogeneous

ous line shape, its contribution is orders of magnitude smaller than the first term and it does not depend on the rf tuning parameter Δ_H . This is so because (i) due to the optical pumping, the normally near-zero Raman population difference $\rho_{22}^0 - \rho_{11}^0$ in the first term of (2.19) is comparable to the population difference $\rho_{33}^0 - \rho_{22}^0$ (or $\rho_{33}^0 - \rho_{11}^0$) in the second term, and (ii) the magnetic inhomogeneous linewidth (~ 100 kHz) is orders of magnitude smaller than the optical inhomogeneous linewidth (~ 5 GHz).

Therefore, denoting the portion of the second-order stationary solutions (2.19) which contribute to the Raman signal by $\tilde{\rho}_{13}^s$ and $\tilde{\rho}_{23}^s$, we have

$$\tilde{\rho}_{13}^s = \frac{\alpha_2\beta e^{i\omega_H t}}{i(\Delta_E + \Delta_H) - \gamma_{13}} \frac{\rho_{22}^0 - \rho_{11}^0}{i\Delta_H - \gamma_{12}}, \quad (2.20a)$$

$$\tilde{\rho}_{23}^s = \frac{\alpha_1 \beta^* e^{-i\omega_H t}}{i(\Delta_E + \omega_H) - \gamma_{23}} \frac{\rho_{22}^0 - \rho_{11}^0}{i\Delta_H + \gamma_{12}}. \quad (2.20b)$$

Note that in cases where the Raman energy separation $\hbar\omega_{21}$ is larger than the Boltzmann factor kT , as in infrared transitions, the population differences in (i) are also comparable even without optical pumping.

C. Raman heterodyne signal

To obtain the Raman signal field \tilde{E}_s (2.6), one averages the signal matrix elements $\tilde{\rho}_{13}^s$ and $\tilde{\rho}_{23}^s$ (2.20) over the Gaussian crystal strain and magnetic inhomogeneous line shapes, $g_E(\Delta_E)$ and $g_H(\Delta_H)$, respectively, given by

$$g_E(\Delta_E) = \frac{1}{\sqrt{\pi}\sigma_E} e^{-[(\Delta_E - \bar{\Delta}_E)/\sigma_E]^2}, \quad (2.21a)$$

and

$$g_H(\Delta_H) = \frac{1}{\sqrt{\pi}\sigma_H} e^{-[(\Delta_H - \bar{\Delta}_H)/\sigma_H]^2}, \quad (2.21b)$$

where $\bar{\Delta}_E \equiv \omega_{32}^0 - \omega_E$, $\bar{\Delta}_H \equiv \omega_{21}^0 - \omega_H$ are the laser-frequency and rf offsets from the center frequencies ω_{32}^0 and ω_{21}^0 of the inhomogeneously broadened transitions $3 \leftrightarrow 2$ and $2 \leftrightarrow 1$, respectively. σ_E and σ_H are the respective half widths at the $1/e$ points of the line shapes g_E and g_H . We assume that the strain broadening is very large and satisfies

$$\sigma_E \gg \sigma_H, \gamma_{i3}, \quad i=1,2. \quad (2.22)$$

Making use of the w function²⁵

$$w(z) = \frac{i}{\pi} \int_{-\infty}^{\infty} \frac{e^{-t^2} dt}{z-t}, \quad \text{Im}z > 0 \quad (2.23a)$$

and its property

$$w(-z^*) = w(z)^*, \quad (2.23b)$$

we compute the average of the signal matrix elements

$$\langle \tilde{\rho}_{i3}^s \rangle = \int_{-\infty}^{\infty} \int_{-\infty}^{\infty} d\Delta_E d\Delta_H g_E(\Delta_E) g_H(\Delta_H) \tilde{\rho}_{i3}^s, \quad i=1,2. \quad (2.24)$$

Noting that the optical inhomogeneous width is large (2.22), the integration over Δ_E is simplified and one obtains

$$\langle \tilde{\rho}_{13}^s \rangle = \frac{\pi}{\sigma_E \sigma_H} \alpha_2 \beta (\rho_{22}^0 - \rho_{11}^0) e^{i\omega_H t} \times w \left[\frac{\bar{\Delta}_E}{\sigma_E} \right] w \left[\frac{\bar{\Delta}_H + i\gamma_{12}}{\sigma_H} \right], \quad (2.25a)$$

$$\langle \tilde{\rho}_{23}^s \rangle = -\frac{\pi}{\sigma_E \sigma_H} \alpha_1 \beta^* (\rho_{22}^0 - \rho_{11}^0) e^{-i\omega_H t} \times w \left[\frac{\bar{\Delta}_E + \omega_H}{\sigma_E} \right] w^* \left[\frac{\bar{\Delta}_H + i\gamma_{12}}{\sigma_H} \right]. \quad (2.25b)$$

The Raman signal polarization $\langle \tilde{P}_s \rangle$ (2.8) consists of an anti-Stokes component $N\mu_{31} \langle \tilde{\rho}_{13}^s \rangle$ and a Stokes component $N\mu_{32} \langle \tilde{\rho}_{23}^s \rangle$. In the case that the strain broadening

σ_E is large compared with the rf ω_H , we have

$$w \left[\frac{\bar{\Delta}_E + \omega_H}{\sigma_E} \right] \simeq w \left[\frac{\bar{\Delta}_E}{\sigma_E} \right], \quad \sigma_E \gg \omega_H, \quad (2.26)$$

and the Stokes and anti-Stokes components have equal amplitude. If $\sigma_E \gg \omega_H$ is not valid, the Raman signal is dominated by either the anti-Stokes component $N\mu_{31} \langle \tilde{\rho}_{13}^s \rangle$, Eq. (2.25a), or the Stokes component $N\mu_{32} \langle \tilde{\rho}_{23}^s \rangle$, Eq. (2.25b), depending on the optical-frequency offset $\bar{\Delta}_E$.

For $\text{Pr}^{3+}:\text{LaF}_3$, the optical inhomogeneous width is large, and (2.26) is satisfied. Then, one obtains from Eqs. (2.7) and (2.8) and the signal matrix elements (2.25) the Raman signal field [Eq. (2.6)],

$$\tilde{E}_s = -\frac{4\pi^2 i \hbar k_E L N}{\sigma_E \sigma_H E_0^*} (\rho_{22}^0 - \rho_{11}^0) w \left[\frac{\bar{\Delta}_E}{\sigma_E} \right] \times \left[\alpha_1^* \alpha_2 \beta w \left[\frac{\bar{\Delta}_H + i\sigma_{12}}{\sigma_H} \right] e^{i\omega_H t} - \text{c.c.} \right], \quad (2.27)$$

where L is the length of an optically thin sample. The Raman heterodyne beat signal I_s Eq. (2.10) is given by

$$I_s = a |E_0|^2 |H_1| (\rho_{22}^0 - \rho_{11}^0) \text{Re} \left[w \left[\frac{\bar{\Delta}_E}{\sigma_E} \right] \right] \times \text{Im} \left[w \left[\frac{\bar{\Delta}_H + i\gamma_{12}}{\sigma_H} \right] e^{i\omega_H t} \right], \quad (2.28)$$

where the constant

$$a = \frac{\pi^2 k_E L N}{\sigma_E \sigma_H \hbar^2} \mu_{12} \mu_{23} \mu_{31}. \quad (2.29)$$

In Eqs. (2.28) and (2.29) the definitions (2.4) of the dipole coupling parameters α_1 , α_2 , and β are used, and the overall phase of the coupling product $\alpha_1^* \alpha_2 \beta$ is set to zero.

For on-resonance optical excitation $\sigma_E \gg \bar{\Delta}_E$, one can use the expansion²⁵

$$w(z) \simeq e^{-z^2} \left[1 + \frac{2iz}{\sqrt{\pi}} \right], \quad z \rightarrow 0 \quad (2.30)$$

to recover the usual Gaussian factor

$$w \left[\frac{\bar{\Delta}_E}{\sigma_E} \right] \simeq e^{-(\bar{\Delta}_E/\sigma_E)^2}, \quad \sigma_E \gg \bar{\Delta}_E. \quad (2.31)$$

One then obtains

$$I_s = a' \chi \chi_1 \chi_2 (\rho_{22}^0 - \rho_{11}^0) e^{-(\bar{\Delta}_E/\sigma_E)^2} \times \left[\cos(\omega_H t) \text{Im} w \left[\frac{\bar{\Delta}_H + i\gamma_{12}}{\sigma_H} \right] + \sin(\omega_H t) \text{Re} w \left[\frac{\bar{\Delta}_H + i\gamma_{12}}{\sigma_H} \right] \right], \quad (2.32)$$

where $a' \equiv \pi^2 k_E N L \hbar / \sigma_E \sigma_H$. We have again used the coupling parameter definitions (2.4) and their relation with the Rabi frequencies [Eq. (2.5)]. Equation (2.32) is identical²⁶ with the expression we have obtained earlier.¹

D. Results of theory

Within the assumptions of the RWA (2.11), weak fields (2.15), and a large optical inhomogeneous width, (2.22) and (2.26), we have obtained the steady-state Raman heterodyne signal I_s (2.28). From Eq. (2.28) we note that the Raman signal is linear in laser power $|E_0|^2$ and in the magnetic field amplitude $|H_1|$, where a factor $|E_0 H_1|$ is required by the two-photon process and heterodyning introduces the second $|E_0|$. It is also linear in each of the three dipole moments $\mu_{12}\mu_{23}\mu_{31}$, Eq. (2.29). This shows clearly that the effect is a three-wave mixing process and that no Raman heterodyne signal is observed unless all three transitions are dipole allowed.

The factor $\rho_{22}^0 - \rho_{11}^0$ in Eq. (2.28) indicates that a population difference between the Raman levels is required in order to have a nonzero Raman signal. Its actual magnitude is determined by optical pumping which occurs on a slow time scale.

The Raman signal I_s can be reduced to a simple expression when we assume large inhomogeneous widths σ_E and σ_H . For a large optical inhomogeneous width one obtains the Gaussian approximation (2.31). For a large magnetic inhomogeneous width $\sigma_B \gg \bar{\Delta}_B$ and also $\gamma_{12} \rightarrow 0$, the expansion (2.30) enables one to obtain

$$\text{Im} \left[w \left[\frac{\bar{\Delta}_H + i\gamma_{12}}{\sigma_H} \right] e^{i\omega_H t} \right] \simeq e^{-(\bar{\Delta}_H/\sigma_H)^2} \left[\sin(\omega_H t) + \frac{2\bar{\Delta}_H}{\sqrt{\pi}\sigma_H} \cos(\omega_H t) \right]. \quad (2.33)$$

With rf phase-sensitive detection, one can therefore select the in-phase dispersive signal $I_s(0^\circ)$ or the out-of-phase absorptive signal $I_s(90^\circ)$ of I_s , Eq. (2.28), given by

$$I_s(0^\circ) = I_s(90^\circ) \frac{2}{\sqrt{\pi}} \left[\frac{\bar{\Delta}_H}{\sigma_H} \right], \quad (2.34a)$$

$$I_s(90^\circ) = a |E_0|^2 |H_1| (\rho_{22}^0 - \rho_{11}^0) \times e^{-(\bar{\Delta}_E/\sigma_E)^2} e^{-(\bar{\Delta}_H/\sigma_H)^2}, \quad (2.34b)$$

where the approximations (2.31) and (2.33) are used and the constant a is given by Eq. (2.29). The absorptive and dispersive signals display the overall magnetic inhomogeneous Gaussian line shape, and one is able to measure the line centers and linewidths of the inhomogeneously broadened rf transition alone. When the conditions $\sigma_B \gg \bar{\Delta}_B$, $\gamma_{12} \rightarrow 0$ are relaxed, the overall absorptive and dispersive line shapes are a convolution of a Gaussian and a Lorentzian line shape, but the essential features of the signals Eq. (2.34) remain the same.

One can write the total field \tilde{E}_T (2.9b) in a manner which reveals explicitly the amplitude-modulation (AM) and frequency-modulation (FM) sideband structure. If ω_0 and ω_m are the carrier and modulation frequencies, respectively, and c and d are the AM and FM modulation depths, we can represent AM by

$$E_{AM} = E_0 [1 + c \cos(\omega_m t + \phi)] e^{i\omega_0 t}, \quad (2.35a)$$

and FM by

$$E_{FM} = E_0 e^{i\omega_0 t} e^{id \cos(\omega_m t + \phi)}. \quad (2.35b)$$

They can be written as

$$E_{AM} = E_0 (1 + u e^{i\omega_m t} + u^* e^{-i\omega_m t}) e^{i\omega_0 t}, \quad (2.36a)$$

and, for small FM modulation depth $d \ll 1$,

$$E_{FM} = E_0 (1 + v e^{i\omega_m t} - v^* e^{-i\omega_m t}) e^{i\omega_0 t}, \quad (2.36b)$$

where the respective complex AM and FM sideband amplitudes are given by

$$u = \frac{1}{2} c e^{i\phi}, \quad (2.36c)$$

and

$$v = \frac{1}{2} d e^{i\phi}. \quad (2.36d)$$

Equations (2.36) show that in AM the sidebands at frequencies $\pm\omega_m$ have the same phase, while those in FM have opposite phase. Hence AM and FM can be distinguished by the phase relationship of the sideband complex amplitudes. The total field \tilde{E}_T (2.9b) can be written as

$$\tilde{E}_T = \frac{1}{2} E_0 (1 + x e^{i\omega_H t} + y e^{-i\omega_H t}) \quad (2.37a)$$

and decomposed into

$$\tilde{E}_T = \frac{1}{2} E_0 [1 + (u e^{i\omega_H t} + \text{c.c.}) + (v e^{i\omega_H t} - \text{c.c.})], \quad (2.37b)$$

with

$$u = \frac{1}{2} (x + y^*)$$

and

$$v = \frac{1}{2} (x - y^*), \quad (2.37c)$$

thus showing the AM (second term) and FM (last term) sideband structure. We can, therefore, obtain from the Raman signal field \tilde{E}_s (2.27) the AM and FM sideband complex amplitudes

$$u(\text{AM}) = q \text{Re} w \left[\frac{\bar{\Delta}_E}{\sigma_E} \right], \quad (2.38a)$$

$$v(\text{FM}) = i q \text{Im} w \left[\frac{\bar{\Delta}_E}{\sigma_E} \right], \quad (2.38b)$$

$$q = \frac{-i\pi^2 k_E L N}{\sigma_E \sigma_H \hbar^2} (\rho_{22}^0 - \rho_{11}^0) (\mu_{12} \mu_{23} \mu_{31}) H_1 \times w \left[\frac{\bar{\Delta}_H + i\gamma_{12}}{\sigma_H} \right]. \quad (2.38c)$$

Equations (2.37) and (2.38) show clearly the simultaneous presence of AM and FM in the total field. In a square-law detector, the FM signal cancels out and only the AM signal (the real part) remains, from which one obtains the

absorptive and dispersive signals [Eq. (2.34)].

When the laser is off-resonant with the optical transition (for $\bar{\Delta}_E \gg \sigma_E$) we obtain²⁵

$$w \left[\frac{\bar{\Delta}_E}{\sigma_E} \right] \sim \frac{i\sigma_E}{\sqrt{\pi}\bar{\Delta}_E}, \text{ for } \bar{\Delta}_E \gg \sigma_E. \quad (2.39)$$

The AM signal (2.38a) is weak, while the FM signal (2.38b) which contains $\text{Im}w(\bar{\Delta}_E/\sigma_E)$ is dominant and therefore can be monitored with the use of an FM-detection scheme. The loss in signal due to the large optical-frequency offset can be compensated for with an increase in laser power. Hence our results predict that the Raman signal can be detected with the use of resonant or nonresonant light in either an AM or FM mode, making it a very versatile technique.

E. A more general solution

Here we seek a time-dependent solution to the equations of motion (2.12) in the limits of a weak optical field

$$\alpha_1, \alpha_2 \rightarrow 0, \quad (2.40a)$$

and a large optical inhomogeneous width

$$\sigma_E \rightarrow \infty, \quad (2.40b)$$

with arbitrary rf-field strength H_1 . From the formal solution for $\tilde{\rho}_{23}(t)$, Eq. (2.13f), the part which contributes to the Raman heterodyne signal is given by

$$\tilde{\rho}_{23}^s(t) = \int_0^t dt' e^{(i\Delta_E - \gamma_{23})(t-t')} e^{-i\omega_H t'} [-i\alpha_1 \tilde{\rho}_{21}(t')], \quad (2.41)$$

with the RWA being the only assumption. Averaging over the inhomogeneous line shapes (2.21), one obtains

$$\langle \tilde{\rho}_{23}^s(t) \rangle = -i\alpha_1 e^{-i\omega_H t} \int g_H(\Delta_H) d\Delta_H \int_0^t dt' \tilde{\rho}_{21}(t') \left[e^{(i\omega_H - \gamma_{23})(t-t')} \int g_E(\Delta_E) d\Delta_E e^{i\Delta_E(t-t')} \right]. \quad (2.42)$$

In Eq. (2.42) the matrix element $\tilde{\rho}_{21}(t')$ is assumed to have no Δ_E dependence, which is valid in the limit of a weak optical field (2.40a). This is evident from the structure of the formal solutions Eqs. (2.13a), (2.13b), and (2.13d), which show that $\tilde{\rho}_{12}$ has no zeroth- or first-order terms in α_1 and α_2 . This implies that the primary signal of $\tilde{\rho}_{12}$ comes from the interaction of the Raman levels 1 and 2 with the magnetic field \bar{H}_1 .

Integrating over $g_E(\Delta_E)$ (2.21a) gives

$$\int_{-\infty}^{\infty} \frac{e^{-[(\Delta_E - \bar{\Delta}_E)/\sigma_E]^2}}{\sqrt{\pi}\sigma_E} e^{i\Delta_E(t-t')} d\Delta_E = e^{-[\sigma_E(t-t')/2]^2} e^{i\bar{\Delta}_E(t-t')}, \quad (2.43)$$

and Eq. (2.42) becomes

$$\langle \tilde{\rho}_{23}^s(t) \rangle = -i\alpha_1 e^{-i\omega_H t} \int d\Delta_H g_H(\Delta_H) \int_0^t dt' \tilde{\rho}_{21}(t') e^{[i(\bar{\Delta}_E + \omega_H) - \gamma_{23}](t-t')} e^{-[\sigma_E(t-t')/2]^2}. \quad (2.44)$$

Invoking the assumption of a large optical inhomogeneous width σ_E (2.40b), the Gaussian factor $\exp\{-[\sigma_E(t-t')/2]^2\}$ is zero unless $t' = t$, thus allowing us to write it as a delta function $\delta(t-t')$. Hence

$$\int_0^t dt' \tilde{\rho}_{21}(t') e^{[i(\bar{\Delta}_E + \omega_H) - \gamma_{23}](t-t')} e^{-[\sigma_E(t-t')/2]^2} = \int_0^1 dt' \rho_{21}(t') e^{[i(\bar{\Delta}_E + \omega_H) - \gamma_{23}](t-t')} \delta(t-t') = \tilde{\rho}_{21}(t), \quad \sigma_E \rightarrow \infty. \quad (2.45)$$

One then obtains

$$\langle \tilde{\rho}_{23}^s(t) \rangle = -i\alpha_1 e^{-i\omega_H t} \int g_H(\Delta_H) \tilde{\rho}_{21}(\Delta_H, t) d\Delta_H, \quad (2.46a)$$

and similarly

$$\langle \tilde{\rho}_{13}^s(t) \rangle = -i\alpha_2 e^{i\omega_H t} \int g_H(\Delta_H) \tilde{\rho}_{12}(\Delta_H, t) d\Delta_H. \quad (2.46b)$$

Substituting (2.46) into (2.8), one obtains from Eqs. (2.6) and (2.7) the time-dependent Raman signal field \tilde{E}_s :

$$\tilde{E}_s(t) = \frac{-2\pi k_E L N}{\hbar} \mu_{13} \mu_{32} E_0 \text{Re} \langle \rho_{12}(t) \rangle_H, \quad (2.47)$$

where

$$\langle \rho_{12}(t) \rangle_H \equiv \int g_H(\Delta_H) \rho_{12}(\Delta_H, t) d\Delta_H, \quad (2.48)$$

and the relation (2.11a) for ρ_{12} is used.

The Raman signal (2.47) thus obtained is derived within the RWA and in the limits of a weak optical field (2.40a) and a large optical inhomogeneous width (2.40b). It is valid for cw or transient excitations and arbitrary magnetic field strength H_1 . Since there is no constraint imposed on the Raman excitation, multiple rf fields with arbitrary field strengths and frequencies can be applied. The laser field acts as a reliable probe which reproduces coherently cw or transient phenomena in the Raman spin levels.

III. CW MEASUREMENTS

A. Review

We present the results of Raman heterodyne measurements made on the lowest (Γ_1) crystal-field states of the zero-phonon $^1D_2 \leftrightarrow ^3H_4$ transition in $\text{Pr}^{3+}:\text{LaF}_3$ at 5925 Å. These electronic singlet states, where the $2J+1$ degeneracy is lifted by the crystal field because of low C_2 Pr^{3+} site symmetry,²⁷ are each split into three doublets ($\pm I_z$) by the

second-order hyperfine interaction^{28,29} and the nuclear electric quadrupole interaction³⁰ of Pr^{3+} ($I = \frac{5}{2}$), as shown in Fig. 1. There are six magnetically inequivalent Pr^{3+} sites.²⁷

Hyperfine interactions in $\text{Pr}^{3+}:\text{LaF}_3$ have been studied by various techniques such as rf-optical double resonance,^{2,3} enhanced and saturated absorption,^{20,31} photon-echo—nuclear double resonance (PENDOR),⁴ and photon-echo modulation.³² In the present study the level splittings as well as the magnetic inhomogeneous line shapes and widths of the rf hyperfine transitions ($I_z = \frac{1}{2} \leftrightarrow \frac{3}{2}$) and ($I_z = \frac{3}{2} \leftrightarrow \frac{5}{2}$) in both $^3\text{H}_4$ ground and $^1\text{D}_2$ excited states are determined with kilohertz precision, about a fivefold improvement over earlier measurements.

The high sensitivity of the Raman heterodyne technique has yielded narrower inhomogeneous linewidths (Table I) than previous measurements^{2-4,17,20,32} which appear to have been instrument limited. The hyperfine splittings (Table I) are fit with the total nuclear quadrupole Hamiltonian²⁹ (3.1) to obtain the quadrupole parameters D and E (Table II) and the eigenstate amplitudes of the hyperfine levels (Table III), where the $^1\text{D}_2$ excited state is found to be strongly mixed (Sec. III D). The observed line shape in Fig. 4(b) is compared to the predictions of our three-level calculation (Sec. II) and a Monte Carlo line-broadening theory,⁹ where agreement is found in both cases. Anomalous line shapes resembling second derivatives are also observed, as shown in Figs. 4(a) and 5, where a pair of symmetrical side lobes appear.

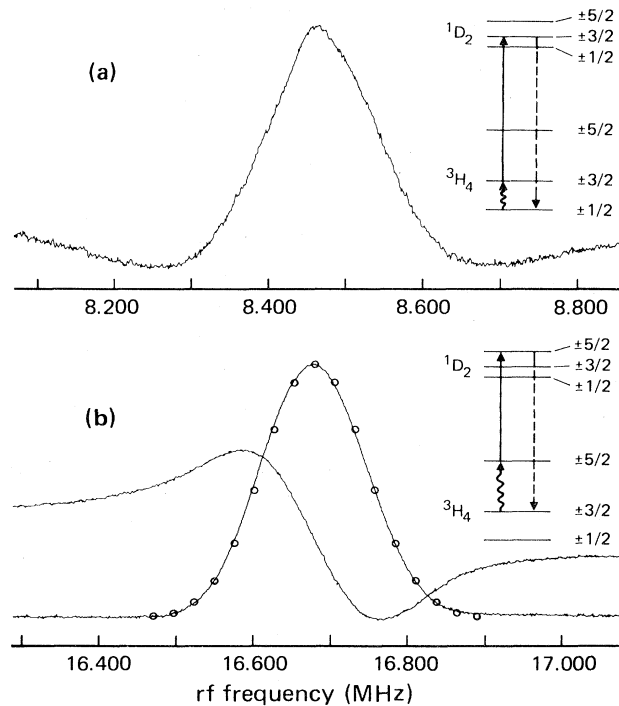


FIG. 4. Raman heterodyne NMR signals of the $\text{Pr}^{3+}:\text{LaF}_3$ $^3\text{H}_4$ ground-state hyperfine transition (a) $I_z = \frac{1}{2} \leftrightarrow \frac{3}{2}$ in absorption for $H_1 = 0.8$ G, and (b) $I_z = \frac{3}{2} \leftrightarrow \frac{5}{2}$ in absorption and dispersion for $H_1 = 0.16$ G in the earth's magnetic field. The open circles represent the Gaussian fit of Eq. (2.34b).

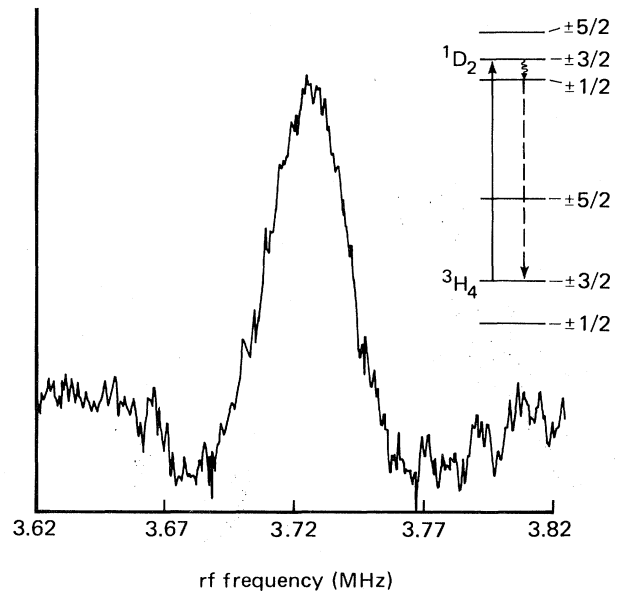


FIG. 5. Raman heterodyne NMR absorptive signal of the $\text{Pr}^{3+}:\text{LaF}_3$ $^1\text{D}_2$ excited-state hyperfine transition $I_z = \frac{1}{2} \leftrightarrow \frac{3}{2}$ in the earth's magnetic field. To avoid rf power broadening, $H_1 = 0.16$ G.

B. Apparatus

A schematic diagram of the apparatus for the cw Raman heterodyne experiment is shown in Fig. 6. A coherent 599 single mode, linearly polarized cw dye laser oscillating in the locked mode (linewidth 4 MHz peak to peak) at 5925 Å excited the $\text{Pr}^{3+} \ ^3\text{H}_4 \leftrightarrow \ ^1\text{D}_2$ transition by propagating along the c axis (also the C_3 axis) of a 0.1-at. % $\text{Pr}^{3+}:\text{LaF}_3$ crystal ($4 \times 4 \times 5$ mm³) with a beam diameter of ~ 100 μm and power in the range 3–50 mW. Radio-frequency magnetic fields H_1 , polarized along the crystal c axis, were applied by a small pair of Helmholtz coils surrounding the crystal, where both were immersed in a liquid-helium cryostat at 1.6 K. Fields up to 3 G in the frequency range $\omega_H/2\pi = 2$ –20 MHz were supplied by Hewlett-Packard model HP3325A frequency synthesizer and an ENI model 400AP broadband rf amplifier. In addition, a static magnetic field H_0 up to 160 G was applied normal to the crystal c axis. The forward scattered laser light was incident upon an E.G.&G. model FND-100 photodiode.

The ac component of the photodiode signal was amplified by a low-noise 47-dB broadband rf amplifier Q-bit QB-256 which was then mixed with the HP3325A local oscillator using a Mini-Circuits Laboratories model ZLW-1-1 double balanced mixer (DBM). The phase of the local oscillator was adjusted to give an absorptive or dispersive Raman signal. An unequal time delay between the Raman signal and the reference at the DBM was avoided as it could distort the signal line shape, caused by a frequency-dependent phase difference between the two inputs.

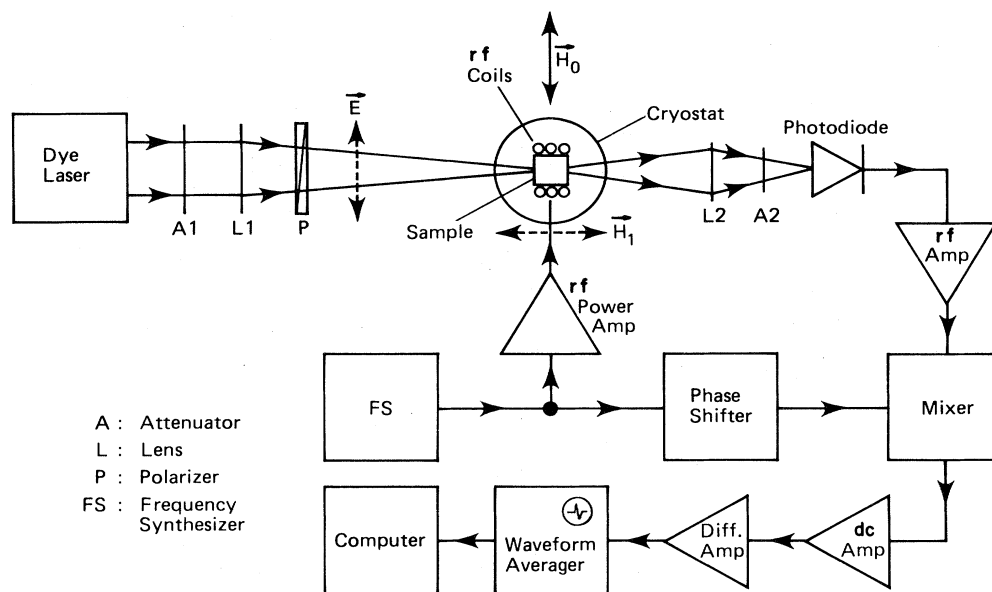


FIG. 6. Schematic of the experimental configuration for cw Raman heterodyne measurements.

The mixer output voltage was amplified 100 times with a two-stage 500-kHz bandwidth dc amplifier, then filtered and amplified again by a Tektronix 7A22 differential amplifier which had a variable bandwidth, set large enough to give an undistorted line shape for a given rf sweep rate. The signal was averaged by a Data Precision 6000 waveform analyzer and model 610 module with 100-kHz 14-bit analog digital conversion. The averaged signal was sent to an IBM personal computer for storage and further analysis.

The Raman signal from the 1D_2 excited-state hyperfine transitions could be observed only if one modified the 3H_4 ground-state optical pumping. This was achieved by externally sweeping the laser frequency (Sec. VB) at a rate ~ 250 MHz per 0.25 s, well within the ~ 5 -GHz optical inhomogeneous line shape. A slower sweep rate reduced the signal size, implying that the optical-pumping cycle was completed within a time ~ 10 ms. Furthermore, we had the option of gating the signal averager so that data could be taken during the positive- or negative-frequency sweep or both. Laser-frequency sweeping was not required for the 3H_4 hyperfine transitions.

In cases where it was necessary to achieve high accuracy for the line centers and linewidths, the experiment was performed under the following conditions. Optical power in the range 3–10 mW was employed so that the Raman signal was in the linear low-power regime according to Eq. (2.28). Saturation of the rf transition was avoided by utilizing low-rf magnetic fields (0.08–0.16 G peak), so that the linewidths were not power broadened and the line centers remained unshifted. Under these conditions, the Raman signal was easily detected as a result of averaging (~ 1000 sweeps) and the high sensitivity of the technique.

We note that the ($I_z = \frac{3}{2} \leftrightarrow \frac{5}{2}$) transition frequencies of both 3H_4 ground and 1D_2 excited states were shifted by -10 kHz at higher rf power ($H_1 \sim 1$ G), whereas the 8.47 and 3.7 MHz resonances did not show any frequency shift.

C. Confirmation of theory

We have confirmed the predictions of the three-level calculations (Sec. IID) in each of the four hyperfine transitions. (i) In the low-power limit, the Raman heterodyne signal is found to depend linearly on the rf-field amplitude H_1 and the laser intensity $|E_0|^2$, Eq. (2.32). (ii) The absorptive and dispersive components of the signal can be obtained by properly adjusting the rf phase ϕ (Fig. 2), as shown in Fig. 4(b), where (iii) the observed absorptive line shape (solid line) of the 16.7-MHz transition is essentially a Gaussian (open circles), Eq. (2.34b), implying that the transition is indeed inhomogeneously broadened.

Table I shows that the two hyperfine transitions ($I_z = \frac{1}{2} \leftrightarrow \frac{3}{2}$) and ($I_z = \frac{3}{2} \leftrightarrow \frac{5}{2}$) have the same low-field linewidths within an electronic level (3H_4 or 1D_2). The linewidths of the 3H_4 ground state (160 kHz) and 1D_2 excited state (32 kHz) scale (~ 5) approximately as the ratio of the gyromagnetic ratios $|\tilde{\gamma}(^3H_4)| / |\tilde{\gamma}(^1D_2)|$. This is expected from theory³³ for a $|\Delta I_z| = 1$ magnetic dipole transition in an inhomogeneous magnetic local field where $|\gamma_z(^3H_4)/(2\pi)| = 10.16$ kHz/G is a low-field result²⁷ but $|\gamma_z(^1D_2)/2\pi| = 3.6$ kHz/G is obtained in the high-field regime,³¹ the ratio being ~ 3 .

At a dc field $H_0 = 30$ – 150 G, the 3H_4 ground-state inhomogeneous widths have been observed to narrow from the zero-field values of 160 to ~ 100 kHz, in agreement

TABLE I. Quadrupole splittings f and comparison of inhomogeneous linewidths Δf (FWHM) for the hyperfine transitions of $^3\text{H}_4$ ground and $^1\text{D}_2$ excited states of 0.1 at. % $\text{Pr}^{3+}:\text{LaF}_3$ in the earth's magnetic field.

$I_z \leftrightarrow I'_z$	f (MHz)	Present study	Δf (kHz)			
			Previous work			
$^3\text{H}_4(\frac{1}{2} \leftrightarrow \frac{3}{2})$	8.470 ± 0.005	166 ± 2	159 ± 5^a	220 ± 30^b	200 ± 10^c	
$^3\text{H}_4(\frac{3}{2} \leftrightarrow \frac{5}{2})$	16.688 ± 0.003	158 ± 2	160.5 ± 1^a	200 ± 30^b	180 ± 10^c	230 ± 25^d
$^1\text{D}_2(\frac{1}{2} \leftrightarrow \frac{3}{2})$	3.724 ± 0.006	32 ± 3	46.5 ± 1^a	70 ± 20^e	200 ± 50^f	
$^1\text{D}_2(\frac{3}{2} \leftrightarrow \frac{5}{2})$	4.791 ± 0.004	33 ± 3	45.3 ± 2.6^a	60 ± 30^e	200 ± 50^f	

^aReference 1, with the use of the Raman heterodyne technique.

^bReference 17.

^cReference 2.

^dReference 3.

^eReference 32.

^fReference 20.

with Monte Carlo (82 kHz) and second-moment (84.5 kHz) line-broadening calculations.⁹ Such a reduction in the static dipolar linewidth when H_0 is increased from its zero value agrees with a second-moment calculation by Abragam and Kambe.³⁴

D. Nuclear quadrupole interaction

In $\text{Pr}^{3+}:\text{LaF}_3$, each electronic level ($^3\text{H}_4$ or $^1\text{D}_2$) is split into three doublets ($\pm I_z$) by the dominant second-order hyperfine interaction^{28,29} and the nuclear electric quadrupole interaction³⁰ of Pr^{3+} ($I = \frac{5}{2}$). The second-order hyperfine interaction, which is determined by the crystal-field splittings and the hyperfine coupling constant, enhances the effective Pr^{3+} nuclear magnetic moment.²⁸ Since the strength of this enhanced, second-order hyperfine interaction differs for each electronic level, the enhanced gyromagnetic tensors of the $^3\text{H}_4$ ground and $^1\text{D}_2$ excited states can vary in magnitude and orientation. The pure nuclear quadrupole interaction and the hyperfine-induced nuclear pseudoquadrupole interaction can be described by a single total nuclear quadrupole Hamiltonian²⁹

$$\mathcal{H}_Q = D[I_z^2 - I(I+1)/3] + E(I_x^2 - I_y^2), \quad (3.1)$$

where each crystal-field state has a different set of quadrupole parameters D and E . We also define an overall asymmetry parameter $\eta \equiv |3E/D|$.

The quadrupole splittings in the earth's field (Table I) obtained by the Raman heterodyne technique can be fit³⁰ with the Pr^{3+} nuclear quadrupole Hamiltonian (3.1), and supply the quadrupole parameters D and E and the asymmetry parameter η for each electronic state. The value of η allows the determination of the amount of state mixing of the hyperfine levels within an electronic state ($^3\text{H}_4$ or $^1\text{D}_2$), which is important for an understanding of the Raman heterodyne effect.

For the $^1\text{D}_2$ excited state 3.724- and 4.791-MHz splittings (Table I), one finds two possible sets of D and E values. One set, where $\eta < 1$, assigns the 3.7-MHz splitting to the ($I_z = \frac{1}{2} \leftrightarrow \frac{3}{2}$) transition, while the other set, with $\eta > 1$, assigns it to the ($I_z = \frac{3}{2} \leftrightarrow \frac{5}{2}$) transition.

The correct set of D and E values can be deduced when one examines the Zeeman splittings under a static magnetic field $H_0 \sim 150$ G perpendicular to the c axis. The ($I_z = \pm \frac{3}{2} \leftrightarrow \pm \frac{5}{2}$) transition is expected to split into two Zeeman lines under H_0 , while the ($I_z = \pm \frac{1}{2} \leftrightarrow \pm \frac{3}{2}$) transition should split into four lines due to the admixture of the $\pm \frac{1}{2}$ states induced by the dc field.^{30,33} Note that the six inequivalent Pr^{3+} sites²⁷ can be grouped into three pairs, where the two sites in each pair are indistinguishable in this study ($H_0 \leq 150$ G perpendicular to the c axis). Thus we have observed 6 lines from the $^1\text{D}_2$ 4.8-MHz transition and 12 lines from the 3.7-MHz transition, corresponding to the respective two and four Zeeman lines of each of the three pairs of Pr^{3+} sites. This observation enables us to assign the 3.7-MHz splitting to the $^1\text{D}_2(I_z = \pm \frac{1}{2} \leftrightarrow \pm \frac{3}{2})$ transition. Similarly in the ground state, we correlate the 8.5-MHz splitting with the ($I_z = \pm \frac{1}{2} \leftrightarrow \pm \frac{3}{2}$) transition. The assignments indicate that $\eta < 1$ for both ground and excited states and determine the correct values of $|D|$ and $|E|$ which are summarized in Table II. Note that the sign of D (or E) cannot be determined from the splittings.

TABLE II. Quadrupole parameters $|D|$, $|E|$, and the asymmetry parameter η of the $\text{Pr}^{3+}:\text{LaF}_3$ nuclear quadrupole Hamiltonian \mathcal{H}_Q [Eq. (3.1)] of the Pr^{3+} $^3\text{H}_4$ ground and $^1\text{D}_2$ excited states.

State	$ D $ (MHz)	$ E $ (MHz)	η
$^3\text{H}_4$	4.1819 ± 0.0013	0.151 ± 0.004	0.108 ± 0.003
$^1\text{D}_2$	1.2938 ± 0.0009	0.305 ± 0.001	0.706 ± 0.002

With the values of $|D|$ and $|E|$ from Table II the quadrupole Hamiltonian (3.1) is diagonalized to yield the zero-field ($H_0=0$ G) eigenstates $|I_z\rangle$ in terms of the pure states ($\eta=0$) $|I_z^0\rangle$:

$$|I_z\rangle = \sum_{I_z=-\frac{5}{2}}^{\frac{5}{2}} a(I_z) |I_z^0\rangle, \quad (3.2)$$

where from Eq. (3.1), $\eta \equiv |3E/D| = 0$ implies that there is no mixing of the hyperfine states. The coefficients $a(I_z)$ are given in Table III. Owing to the large asymmetry parameter $\eta(^1D_2) = 0.706$, the significance of state mixing in 1D_2 is apparent. The mixing of $|I_z^0\rangle$ in the excited state therefore makes possible the electric dipole $^1D_2 \leftrightarrow ^3H_4$ optical transition when $\Delta I_z \neq 0$, and gives rise to the Raman heterodyne signal, which requires that all three transitions be active [Eq. (2.29)].

We note that the present ground-state quadrupole parameters (Table II) and eigenstate amplitudes $a(I_z)$ (Table III) are in agreement with those obtained by Erickson.² However, Erickson has chosen the other set of $|D|$ and $|E|$ values for the 1D_2 excited state ($\eta > 1$).²⁰

E. Inhomogeneous linewidths and line shapes

Table I compares the present measurements with previous values of the inhomogeneous widths of the ground- and excited-state hyperfine transitions in the earth's field. The 1D_2 excited-state linewidths [full width at half maximum (FWHM)] of 32 ± 3 kHz are much narrower than Erickson's measurement²⁰ (200 ± 50 kHz), which presumably is limited by laser-frequency stability. They are also narrower than our previous Raman heterodyne measurement¹ (46 ± 3 kHz) and those of Whittaker and Hartmann³² (60 ± 20 kHz). Our current linewidths are obtained by using lower rf fields ($H_1 = 0.16$ G) to avoid saturation, and by synchronizing the averaging process to the direction of the laser-frequency sweep so that either positive or negative frequency sweep signals are averaged but not both. The procedure is important because laser sweeping prepares the 1D_2 populations differently depending on the sweep direction (Sec. V B) and asynchronous signal averaging can contribute a few kilohertz to the linewidth.

The present ground-state 8.47- and 16.7-MHz transition linewidths (Table I) are in agreement with our previous values¹ (160 kHz), which are also narrower than earlier measurements.^{2,3,17} The weak excited-state sum frequency ($I_z = \frac{1}{2} \leftrightarrow \frac{5}{2}$) 8.51-MHz resonance observed in photon-echo modulation³² does not appear in the ground-state 8.47-MHz line shape of Fig. 4(a). This is because the laser is not swept during the ground-state measurement, and optical pumping greatly reduces the population in the excited state, thus making the 8.51-MHz resonance too weak to be detected.

The 3H_4 8.47-MHz transition in Fig. 4(a) and the 1D_2 3.7-MHz transition in Fig. 5 do not conform to a Gaussian line shape but more closely resemble a second derivative due to the presence of a pair of symmetrical side lobes. Although the nature of the side lobes is not understood, we have determined some of their characteristics, in particular those of the 8.47-MHz transition. In contrast, the 4.8-MHz line shape exhibits, to a lesser degree, a similar side-lobe structure, but the 16.7-MHz resonance of Fig. 4(b) exhibits a pure Gaussian line shape with no side lobes whatsoever.

We have tried unsuccessfully to eliminate the 8.47-MHz side lobes in Fig. 4(a) by (1) applying 3.7-MHz and/or 4.8-MHz rf fields (to check the presence of the excited-state sum frequency 8.51-MHz resonance), (2) applying a 16.7-MHz rf field (0–3 G, to modify the optical-pumping cycle), (3) applying a static magnetic field (0–20 G), (4) changing the rf-sweep rate (0.01–1 s), (5) rf power (0.08–5 G), and (6) laser power (3–40 mW). These tests modify the anomalous line shape only to the extent of a change in the signal size or an overall phase shift.

An interesting effect has been observed in the 1D_2 4.8-MHz resonance when a small dc field is applied. As H_0 is increased from zero, the signal decreases initially and reaches a minimum (~ 5 times smaller) at $H_0 = 3.3$ G (greater than the earth's field of ~ 0.5 G). Further increase of H_0 reverses the phase of the signal, which starts to increase in magnitude. At $H_0 = 6.2$ G, it reaches a signal size about the same as that at $H_0 = 0$ G. A similar behavior in the 8.47-MHz resonance has also been observed. This observation suggests that the anomalous line shapes in Figs. 4(a) and 5 may be related in a complicated way to the local magnetic fields due to the ^{19}F nuclei,

TABLE III. Amplitudes $a(I_z)$ of eigenstates $|I_z\rangle$ in terms of pure states ($\eta=0$) $|I_z^0\rangle$ of $\text{Pr}^{3+}:\text{LaF}_3$ 3H_4 ground and 1D_2 excited states.

	$ I_z\rangle$	$ \pm \frac{5}{2}\rangle$	$ \pm \frac{1}{2}\rangle$	$ \mp \frac{3}{2}\rangle$
3H_4	$ \pm \frac{5}{2}\rangle$	0.999 82	0.019 02	0.000 73
	$ \pm \frac{1}{2}\rangle$	−0.018 91	0.996 95	−0.075 75
	$ \mp \frac{3}{2}\rangle$	−0.002 17	0.075 73	0.997 13
1D_2	$ \pm \frac{5}{2}\rangle$	0.991 54	0.126 13	0.030 76
	$ \pm \frac{1}{2}\rangle$	−0.105 88	0.922 75	−0.370 58
	$ \mp \frac{3}{2}\rangle$	−0.075 12	0.364 19	0.928 29

which are modified by the application of a small dc field. Further studies in this system and other impurity-ion solids should illuminate the exact nature of these side lobes.

IV. COHERENT SPIN TRANSIENTS

A. Motivation

As is well known, coherent spin transients³³ are useful for the study of nuclear time-dependent phenomena. In $\text{Pr}^{3+}:\text{LaF}_3$, the ^{19}F - ^{19}F spin-flip fluctuations^{5,7} are responsible for the dephasing of both the optical and hyperfine transitions. Therefore, it is of interest to obtain homogeneous widths of the hyperfine transitions not only in the ground state but also in the optically excited state, thus allowing a comparison with the optical homogeneous linewidth.⁵⁻⁸

Previous transient studies of Pr^{3+} hyperfine transitions have been confined to the ground state.³ The Raman heterodyne technique has enabled us to observe spin echoes (Fig. 7), free-induction decay (FID), and nutation (Fig. 8) of each hyperfine transition in both $^3\text{H}_4$ ground and $^1\text{D}_2$ excited electronic levels. Spin-echo measurements have yielded homogeneous linewidths for the four rf transitions (Table IV), which are compared for the first time with the homogeneous width of the $^3\text{H}_4 \leftrightarrow ^1\text{D}_2$ optical transition. Coherent spin transients have also allowed us to (i) measure the gyromagnetic ratio γ_x by spin nutation (Sec. IV D), and (ii) observe an interference effect of the echo amplitude when the delay time is small (Fig. 9).

B. Apparatus

For the transient Raman measurements, the optical arrangement of Fig. 6 remained the same while a different electronics configuration was required, as shown in Fig. 10. Proper impedance matching of the rf input to the resonant Helmholtz coils yielded up to 65 G of pulsed rf fields which were derived from a gated HP3325A frequency synthesizer and followed by a broadband rf power amplifier ENI350L. The gate was a home-built multiple-pulse generator capable of producing pulses of variable widths (1–100 μs) with digitally controlled pulse separations, and was also used in the detection process described below.

The ac component of the photodiode signal was filtered with a bandpass filter centered at the rf transition frequency (3–17 MHz) with ~ 1 MHz full width at -3 dB, and was amplified by an rf amplifier Q -bit QB-256. In spin-echo measurements, the nutation signal was attenuated by a gated current controlled DBM but the echo was not, providing an effective gain of a factor of ~ 10 on the echo. This put the nutation and echo on the same vertical scale so that in the analysis the echo amplitude could be calibrated with respect to the first pulse nutation, a procedure that was required due to the laser-power fluctuation from one pulse sequence to the next. The rf signal was then amplified by a Q -bit QB-188 amplifier before being mixed with a local oscillator derived from a second HP3325A frequency synthesizer (FS2), which was phased

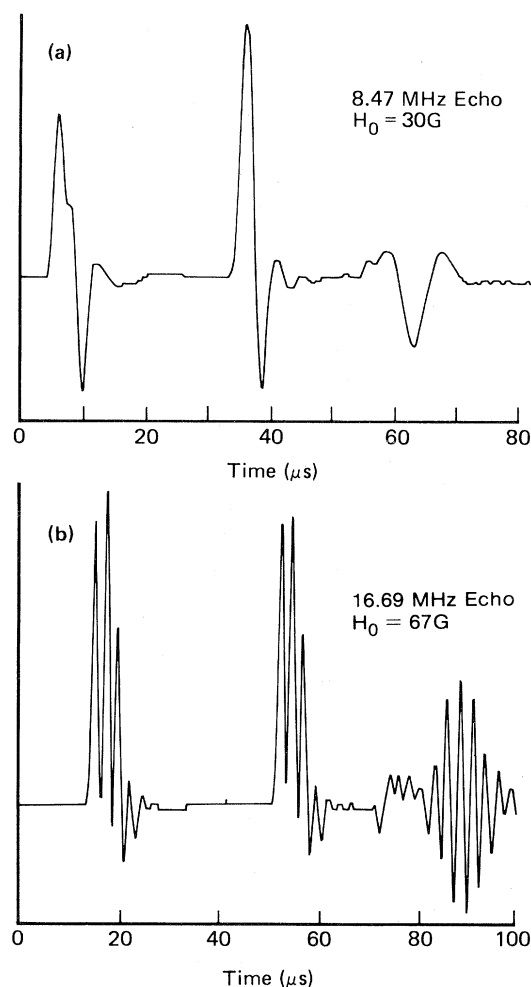


FIG. 7. Raman heterodyne detected spin echoes for (a) the $^3\text{H}_4(I_z = \frac{1}{2} \leftrightarrow \frac{3}{2})$ spin transition where $H_0 = 30$ G, $H_1 = 36$ G, pulse delay time $\tau = 30$ μs , and the rf pulse widths are 3.5 and 2.5 μs , and (b) the $^3\text{H}_4(I_z = \frac{3}{2} \leftrightarrow \frac{5}{2})$ spin transition where $H_0 = 67$ G, $H_1 = 27$ G, $\tau = 38$ μs , and the rf pulse widths are 1.3 and 1.3 μs . In (b) the FID and echo are modulated at the Zeeman frequency 390 ± 10 kHz. The echoes in (a) and (b) are amplified ~ 10 times.

locked to the first one (FS1) and was used here as a convenient and accurate phase shifter. The relative phase of the two synthesizers was adjusted to yield the in-phase or out-of-phase component of the mixer signal, which was then fed through the 500-kHz bandwidth dc amplifier and averaged with a Tektronix 468 digital storage oscilloscope (bandwidth: 10 MHz). The averaged signal was sent to the computer for further analysis

The pulse nature of the transient signal required a large detection bandwidth (~ 500 kHz) so that signal averaging was often necessary. In the excited-state measurements, laser-frequency sweeping was required as described in Sec. III B. The FID and echo were observed to be out of phase with the nutation, as predicted by theory,²¹ which is

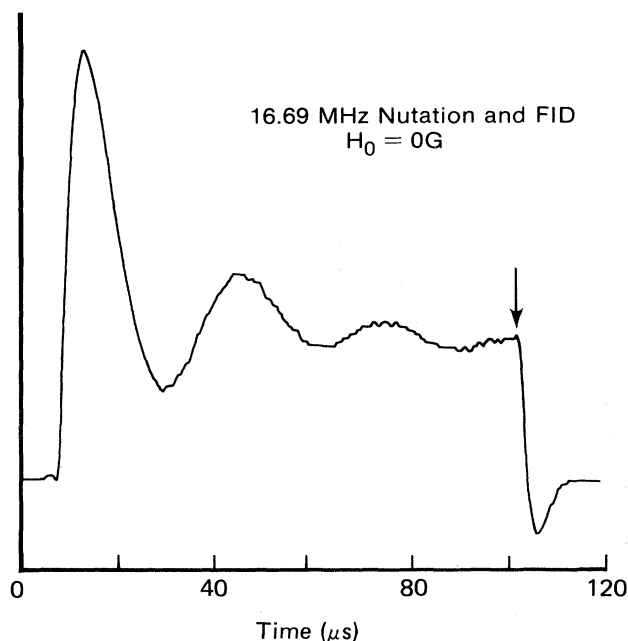


FIG. 8. Raman-detected spin nutation and FID for the ${}^3\text{H}_4(I_z = \frac{3}{2} \leftrightarrow \frac{5}{2})$ 16.69-MHz spin transition where $H_0 = 0$ G, $H_1 = 6.4$ G, rf pulse width equals $100 \mu\text{s}$, with a measured Rabi frequency $\chi/2\pi = \mu_x H_1 / \hbar = 33$ kHz. The arrow marks the end of the applied rf pulse and therefore the beginning of the FID.

shown in a spin echo of the 8.5-MHz transition [Fig. 7(a)] and in the nutation and FID of the 16.7-MHz transition (Fig. 8).

In a spin-echo experiment an rf pulse sequence of $\sim\pi/2$ and $\sim\pi$ was applied with field strength $H_1 = 25\text{--}65$ G parallel to the c axis. The two rf pulses had variable widths ($1\text{--}4 \mu\text{s}$) and were separated by a digitally controlled delay time ($4\text{--}70 \mu\text{s}$). When a dc field $\vec{H}_0 \perp c$ axis of strength greater than 15 G was applied, the optical-pumping cycle was modified and the transients of the 3.7-, 4.8-, and 8.5-MHz transitions were enhanced by a

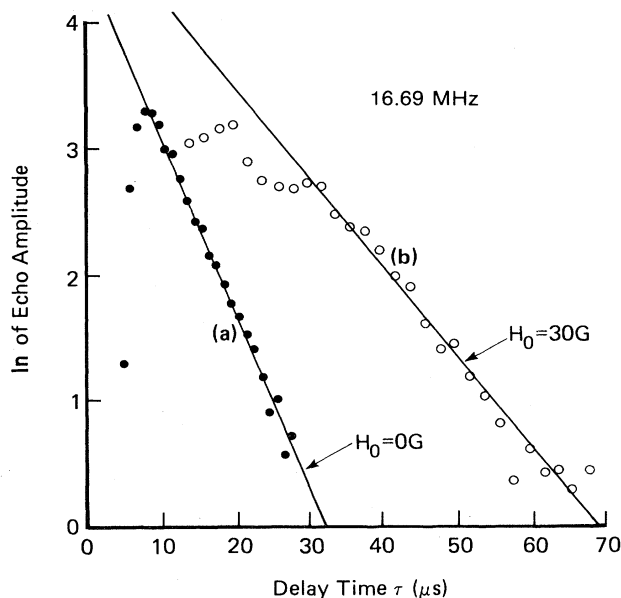


FIG. 9. Natural log of the Raman-detected spin-echo amplitude as a function of the pulse delay time τ for the ${}^3\text{H}_4(I_z = \frac{3}{2} \leftrightarrow \frac{5}{2})$ spin transition for (a) $H_0 = 0$ G indicating a homogeneous linewidth (FWHM) $\Delta f_H = 21 \pm 2$ kHz and (b) $H_0 = 30$ G with $\Delta f_H = 11 \pm 1$ kHz. The signal "bending over" in (a) $\tau \lesssim 8 \mu\text{s}$ and (b) $\tau \lesssim 30 \mu\text{s}$ is due to an interference effect between the echo and FID of the second pulse.

factor of $\sim 5\text{--}10$. At $H_0 = 0$ G, spin echoes were observed only in the 16.7-MHz transition.

Figure 7(b) shows an echo signal of the 16.7-MHz transition at a high dc field $H_0 = 67$ G, where both the FID and echo are modulated at the Zeeman frequency 390 ± 10 kHz. A cw spectrum of the 16.7-MHz transition in the same field reveals that one of the three pairs of Pr^{3+} sites is Zeeman split by ± 390 kHz. Contribution to the echo signal from the other Zeeman lines was suppressed due to the narrow Fourier frequency range of excitation (pulse widths of $1\text{--}4 \mu\text{s}$) and the site-selective laser polarization.^{27,35}

TABLE IV. Homogeneous linewidths Δf_H (FWHM) of hyperfine transitions with quadrupole splittings f for the ${}^3\text{H}_4$ ground and ${}^1\text{D}_2$ excited states of 0.1 at. % $\text{Pr}^{3+}:\text{LaF}_3$ in a dc magnetic field $H_0 \perp c$.

$I_z \leftrightarrow I'_z$	f (MHz)	Δf_H (kHz) ^a	$H_0 \perp c$ (G)
${}^3\text{H}_4(\frac{1}{2} \leftrightarrow \frac{3}{2})$	8.470	19.5 ± 2	~ 30
${}^3\text{H}_4(\frac{3}{2} \leftrightarrow \frac{5}{2})$	16.688	21 ± 2^b	0
${}^3\text{H}_4(\frac{5}{2} \leftrightarrow \frac{7}{2})$	16.688	11 ± 1	$\sim 30\text{--}70$
${}^1\text{D}_2(\frac{1}{2} \leftrightarrow \frac{3}{2})$	3.724	$20 \pm 2^{b,c}$	$\sim 30\text{--}70$
${}^1\text{D}_2(\frac{3}{2} \leftrightarrow \frac{5}{2})$	4.791	15 ± 2	~ 30
${}^1\text{D}_2(\frac{5}{2} \leftrightarrow \frac{7}{2})$	4.791	10 ± 2^d	~ 30

^aMeasurements made with no optical gating as described in Sec. IV B, unless otherwise noted.

^bIdentical results achieved with or without gating sequence (ii) of the laser amplitude as described in Sec. IV F.

^cIdentical results achieved with or without gating sequence (iii) of the laser amplitude, as described in Sec. IV F.

^dWith gating sequence (iii) of the laser amplitude, as described in Sec. IV F.

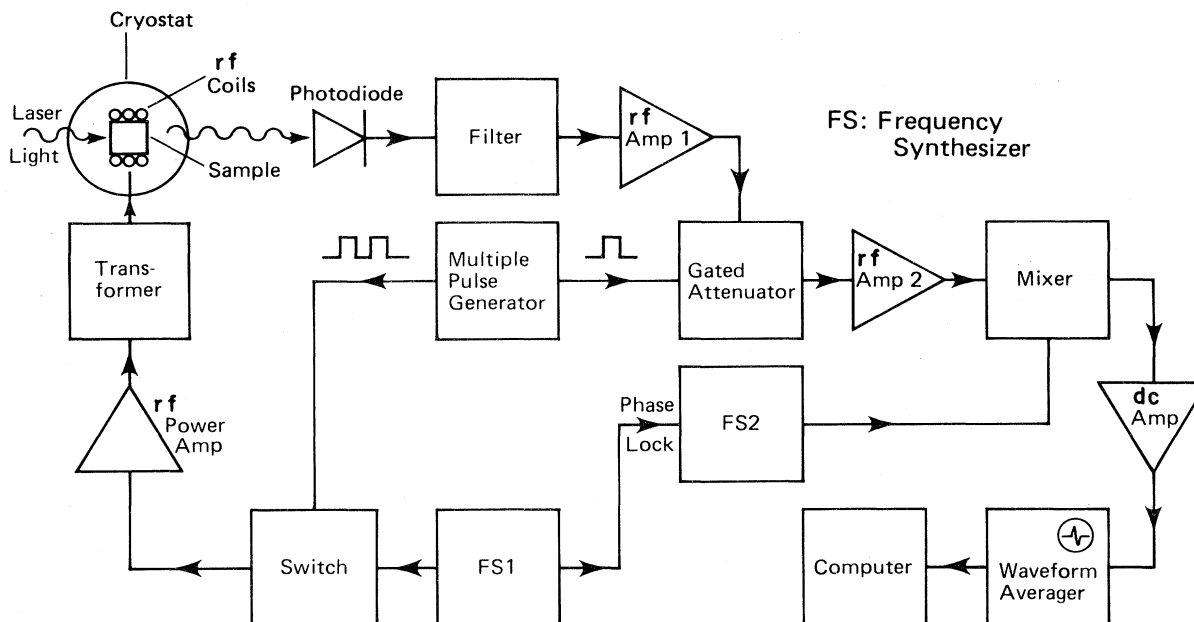


FIG. 10. Schematic of the experimental configuration for coherent spin transient measurements using Raman heterodyne detection.

C. Homogeneous linewidth results

Table IV summarizes the results of spin-echo measurements for the two hyperfine transitions ($I_z = \frac{1}{2} \leftrightarrow \frac{3}{2}$) and ($I_z = \frac{3}{2} \leftrightarrow \frac{5}{2}$) in both ${}^3\text{H}_4$ ground and ${}^1\text{D}_2$ excited states under different experimental conditions (dc field strength and gating of laser field). Figure 9 compares the homogeneous linewidths (FWHM) $\Delta f_H = 1/\pi T_2$ of the 16.7-MHz transition at (a) $H_0 = 0$ G (21 ± 2 kHz) and (b) $H_0 = 30$ G (11 ± 2 kHz), showing a factor of 2 difference in the linewidth. The linewidth of 21 ± 2 kHz at $H_0 = 0$ G agrees with that of Shelby and co-workers³ (19 kHz, $H_0 = 0$ G). We have found no variation in the 16.7-MHz transition linewidth when dc fields in the range 30–70 G are applied in the echo measurements. This implies that $H_0 = 30$ G is sufficient for the linewidth reduction.

In a dc field $H_0 \geq 30$ G, the ${}^{19}\text{F}$ nuclei are quantized along $H_0 \perp c$ axis, rather than the local fields due to the ${}^{141}\text{Pr}$ and other ${}^{19}\text{F}$ nuclei. Under such a condition, the nonsecular terms of the ${}^{19}\text{F}$ - ${}^{141}\text{Pr}$ dipolar Hamiltonian are small³⁴ and therefore there is a corresponding reduction in the ${}^{19}\text{F}$ - ${}^{141}\text{Pr}$ dipolar interaction. This in turn narrows the homogeneous linewidth, as is demonstrated in the 16.7-MHz transition (Fig. 9).

Table I shows that the inhomogeneous widths of the hyperfine transitions for $H_0 = 0$ G are the same within an electronic level (160 kHz for ${}^3\text{H}_4$ and 32 kHz for ${}^1\text{D}_2$), but spin-echo measurements at $H_0 = 30$ G (Table IV) show narrower linewidths for the ($I_z = \frac{3}{2} \leftrightarrow \frac{5}{2}$) transitions (11 kHz for ${}^3\text{H}_4$ and 15 kHz for ${}^1\text{D}_2$) than the ($I_z = \frac{1}{2} \leftrightarrow \frac{3}{2}$) transitions (20 kHz for both ${}^3\text{H}_4$ and ${}^1\text{D}_2$). It is also noted that while the ${}^3\text{H}_4$ and ${}^1\text{D}_2$ inhomogeneous widths scale

approximately as their gyromagnetic ratios (Sec. III C), there is no such relationship in the homogeneous linewidth measurements. The Monte Carlo calculation⁹ points out that such a linear scaling is not expected.

Last of all, it is noted that photon-echo measurements at $H_0 = 80$ G perpendicular to the c axis on the ${}^1\text{D}_2 \leftrightarrow {}^3\text{H}_4$ optical transition by gated heterodyne detection give an optical homogeneous linewidth (FWHM) of ~ 14 kHz.^{6,8} This value of ~ 14 kHz is in agreement with the ${}^1\text{D}_2$ and ${}^3\text{H}_4$ NMR linewidths (~ 10 – 20 kHz). There is clearly a close link between the optical and NMR measurements, but a proper theory has yet to be developed to make such a connection.

D. Nutation and FID

The gyromagnetic ratio $\bar{\gamma}$ for the ground and excited electronic states can be obtained from spin nutation measurements. They can be compared to reveal the amount of enhancement of the Pr^{3+} nuclear magnetic moment due to the second-order hyperfine interaction.²⁸

Spin nutation and FID are observed when a single rf pulse H_1 at the transition frequency is applied along the crystal c axis, which coincides with the C_3 axis. From the Rabi frequency χ one can measure the magnetic dipole moment $\mu_x = \hbar\chi/H_1$ and deduce the gyromagnetic ratio γ_x from the relation

$$\mu_x \equiv \gamma_x \hbar \langle I_x \rangle. \quad (4.1)$$

Here we follow Erickson's convention that the Pr^{3+} site axis, which coincides with the crystal C_3 axis, is the x axis.²⁷

Figure 8 shows a nutation and FID signal of the ground-state 16.7-MHz transition at $H_0=0$ G when a single 100- μ s rf pulse with $H_1=6.4$ G is applied. The nutation is fit with a zero-order Bessel function $J_0(\chi t)$ (Ref. 21) to obtain the Rabi frequency $\chi/2\pi=\mu_x H_1/h$ (33 kHz) to within 5%. From nutation measurements at $H_0=0$ G with different rf-field strength H_1 (5–20 G), we obtain the magnetic dipole moments $\mu_x/h=\chi/2\pi H_1\sim 5.2$, ~ 1.6 , and ~ 2.0 kHz/G for the 16.7-, 4.8-, and 3.7-MHz transitions, respectively. Measurements at $H_0\neq 0$ G show a variation in the dipole moments of less than 10% for H_0 up to 110 G.

Owing to hyperfine state mixing, it is necessary to compute the expectation value $\langle I_x \rangle$ for the 16.7-, 4.8-, and 3.7-MHz transitions, with the use of the eigenstate amplitudes $a(I_z)$ in Table III, in order to obtain from Eq. (4.1) $\gamma_x/2\pi(^3\text{H}_4)=4.55$ kHz/G, and $\gamma_x/2\pi(^1\text{D}_2)=1.3$ kHz/G. The uncertainty ($\sim 10\%$) of γ_x is due to the accuracy of the determination of the Rabi frequencies and the rf-field amplitudes. Therefore, the Pr^{3+} nuclear dipole moment in the $^3\text{H}_4$ ground state is enhanced ~ 3.5 times relative to that in the $^1\text{D}_2$ excited state, which is approximately the same as the bare Pr^{3+} nuclear moment.^{29,36}

Within experimental error our $\gamma_x/2\pi(^3\text{H}_4)$ value is consistent with Erickson's 4.98 ± 0.04 kHz/G obtained by a measurement of the ground-state Zeeman splitting,²⁷ and that of Macfarlane and Shelby (4.2 kHz/G) by nutation at $H_0=0$ G.^{3,31} In contrast, our measured $\gamma_x/2\pi(^1\text{D}_2)=1.3$ kHz/G differs from that (2.20 ± 0.1 kHz/G) of Macfarlane and Shelby, obtained from a high-field study.³¹

E. Interference effect in spin-echo measurements

In Fig. 9(a), the natural logarithm of the echo amplitude of the 16.7-MHz transition at $H_0=0$ G is plotted as a function of the pulse decay time τ . Note that the signal "bends" over near the time origin. Similarly, the same effect occurs at $H_0=30$ G in Fig. 9(b), where the bending extends to a longer delay time (~ 30 μ s). This feature is due to an interference between the echo and the FID of the second pulse when they overlap in time. This interference limits the minimum delay time between the two excitation pulses, and has been observed in echoes of the other hyperfine transitions. To reduce this interference for echo measurements, the dc field is made inhomogeneous by placing a small bar magnet near the sample, creating a field gradient at the crystal. We note that Shelby *et al.* have observed a similar structure in the 16.7-MHz transition echo measurement using a different rf-optical detection scheme.³

The oscillation in Fig. 9(b) occurs because the FID is modulated due to the Zeeman splitting at $H_0=30$ G. The much longer-lived FID-echo interference in Fig. 9(b) ($H_0=30$ G) suggests a longer T_2 dephasing time of the FID, which is confirmed by the narrowing of the linewidth from 21 kHz ($H_0=0$ G) to 11 kHz (30 G).

F. Optical effects in spin-echo measurements

To test how the NMR linewidth measurement is affected by the presence of the optical field, we have used an

acousto-optic modulator to gate the laser amplitude with different gating sequences. (i) An echo signal is observed when the laser field is turned off just before the first rf pulse and on just before the echo, indicating that the laser is not required for the formation of the spin echo. (ii) Similarly, when the laser field is turned off just after the first rf pulse and on just before the echo, T_2 measurements of the 3.7-MHz transition at $H_0=30$ G and the 16.7-MHz transition at $H_0=0$ G (Table IV) show no change in the linewidths. This implies that for these two transitions when the laser is on during an rf pulse sequence, there is no optical power broadening in the NMR homogeneous widths. This procedure (see Sec. IV B) was also used for echo-amplitude calibration.

(iii) We have made linewidth measurements of the $^1\text{D}_2$ excited-state hyperfine transitions with the laser turned on 200 μ s before and off 200 μ s after the rf pulse sequence, at a repetition rate of 30 Hz. Table IV shows that there is no change in linewidth for the 3.7-MHz ($I_z=\frac{1}{2}\leftrightarrow\frac{3}{2}$) transition with optical gating, but the 4.8-MHz ($I_z=\frac{3}{2}\leftrightarrow\frac{5}{2}$) linewidth is reduced from 15 ± 2 to 10 ± 2 kHz. The present results are preliminary, and further studies in this system and other impurity-ion solids are planned to determine the nature of this line-narrowing effect.

V. OPTICAL PUMPING

Optical pumping^{2,20} occurs in $\text{Pr}^{3+}:\text{LaF}_3$ when the population of a ground-state Pr^{3+} hyperfine level is transferred to other hyperfine levels in the $^3\text{H}_4$ ground state via excitation to the $^1\text{D}_2$ hyperfine levels with subsequent relaxation ($\Delta I_z\neq 0$). This action creates a non-thermal ground-state nuclear population distribution that yields nonvanishing Raman signals [Eq. (2.28)] of the ground state, as discussed in the theoretical treatment, Sec. II B. On the other hand, the $^1\text{D}_2$ excited-state Raman signals are observed only when this optical-pumping cycle is modified by laser-frequency sweeping.

A. Effect of ground-state spin-lattice relaxation

According to the studies of Shelby, Macfarlane, and Yannoni,³⁷ for a 0.1-at. % $\text{Pr}^{3+}:\text{LaF}_3$ sample, the experimentally deduced spin-lattice relaxation times T_1^* of the ground-state 8.5- and 16.7-MHz transitions at 1.6 K in the earth's magnetic field are, respectively, 5 and 100 s. The faster T_1^* time for the 8.5-MHz ($I_z=\frac{1}{2}\leftrightarrow\frac{3}{2}$) transition is attributed to a Pr-La cross-relaxation energy-conserving process involving simultaneous spin flips of a Pr nucleus and three surrounding La nuclei. The long spin-lattice relaxation time of the 16.7 MHz ($I_z=\frac{3}{2}\leftrightarrow\frac{5}{2}$) transition is assumed to be due to Pr-Pr interaction.

In a cw measurement at $H_0=0$ G for the $^3\text{H}_4$ 8.5-MHz ($I_z=\pm\frac{1}{2}\leftrightarrow\pm\frac{3}{2}$) transition, population in these levels is optically pumped to the $^3\text{H}_4(I_z=\pm\frac{5}{2})$ hyperfine states and remains there due to the long ($I_z=\pm\frac{5}{2}$) relaxation time ($T_1^*\sim 100$ s), thus reducing the Raman signal. Similarly, in a cw measurement of the $^3\text{H}_4$ 16.7-MHz ($I_z=\pm\frac{3}{2}\leftrightarrow\pm\frac{5}{2}$) transition, population is optically pumped to the $^3\text{H}_4(I_z=\pm\frac{1}{2})$ states. But here the relaxation from ($I_z=\pm\frac{1}{2}$) to ($I_z=\pm\frac{3}{2}$) is faster due to the shorter relaxa-

tion time ($T_1^* \sim 5$ s) of the 8.5-MHz transition, and therefore the Raman signal of the 16.7-MHz transition should be stronger than that of the 8.5-MHz transition. Such a difference in signal size has been observed. Based on this model, one can make the following predictions.

(i) An increase in the 8.5-MHz transition Raman signal ($H_0=0$ G) should occur upon the application of a 16.7-MHz rf field which transfers the optically-pumped population in $I_z = \pm \frac{5}{2}$ to the Raman level $I_z = \pm \frac{3}{2}$. (ii) A similar signal increase of the 8.5-MHz transition ($H_0=0$ G) should also occur if both ground-state hyperfine transitions are excited in a single rf sweep, which redistributes the hyperfine population within a time equal to the rf sweep time (less than T_1^*).

In the present study observations have been made which agree with the predictions (i) and (ii). At $H_0=0$ G, the 8.5-MHz cw Raman signal increases by a factor of ~ 5 when (i) a 16.7-MHz rf field (~ 1 G) is applied, or when (ii) both ground-state hyperfine transitions (8.5 and 16.7 MHz) are excited in a single rf sweep (sweep time equal to 10 ms). In addition, a similar increase is observed when (iii) a dc field $H_0 > 10$ G is applied, which quenches the Pr-La cross-relaxation process³⁷ and mixes the ground-state hyperfine states.

In (ii) as we vary the rf-sweep time from 10 ms to 10 s, the signal size decreases and its phase changes. Figure 11 shows four cw Raman signals each with a different sweep time. When the sweep time varies from (a) 10 ms to (b) 100 ms, the relative size of the 8.5-MHz side lobes changes slightly due to a phase change of the signal. As the sweep time is increased to (c) 1 s, the order of T_1^* of the 8.5-MHz transition, the signal size of both transitions is reduced $\sim 50\%$ and $\sim 20\%$ for the 8.5- and 16.7-MHz transitions, respectively. The 8.5-MHz signal has a larger reduction and its line shape changes more dramatically. When the sweep time approaches the relaxation time of the 16.7-MHz transition, (d) 10 s, the signal size decreases further by $\sim 70\%$ and $\sim 50\%$ for the 8.5- and 16.7-MHz transitions, respectively, and the line shape of the 16.7-MHz transition also starts to change more.

Figure 11 shows that the line shape depends quite critically on the optical-pumping cycle, as modified by the rf-sweep times. However, we note that the basic features of the Raman signal, as described in Sec. II, remain the same. We should mention that within the optical inhomogeneous line, optical pumping can modify the population difference $\rho_{22}^0 - \rho_{11}^0$ in Eq. (2.20) differently, in sign and magnitude, depending on the laser-frequency detuning. Therefore, in the integration over the optical inhomogeneous line shape Eq. (2.24), one cannot assume that $\rho_{22}^0 - \rho_{11}^0$ is constant, and the effect is that the Raman signal phase and magnitude in Eq. (2.28) are modified.

B. Laser-frequency sweeping

In Secs. III B and IV B, it was mentioned that laser-frequency sweeping was used to redistribute the ground-state population resulting from optical pumping, and this allowed detection of excited-state Raman heterodyne signals. In a sweep cycle the hole that is burned in a particular frequency packet within the ~ 5 -GHz optical inhomogeneous

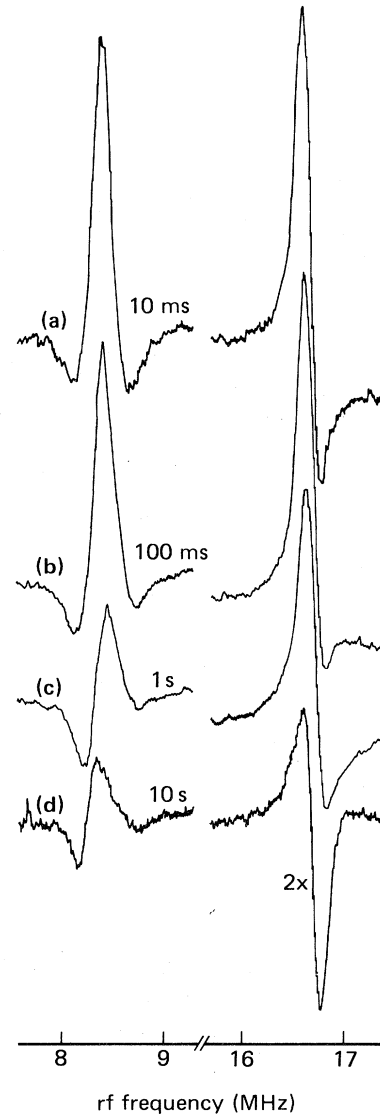


FIG. 11. Raman heterodyne signals of the $\text{Pr}^{3+}:\text{LaF}_3$ ${}^3\text{H}_4(I_z = \frac{1}{2} \leftrightarrow \frac{3}{2})$ and ${}^3\text{H}_4(I_z = \frac{3}{2} \leftrightarrow \frac{5}{2})$ spin transitions at $H_0=0$ G when both transitions are excited in a single rf sweep (7–18 MHz) with the sweep time of (a) 10 ms, (b) 100 ms, (c) 1 s, and (d) 10 s. In (d) the signal is amplified 2 times.

line shape during the positive sweep is refilled in the negative sweep. As a concrete example, consider the ${}^1\text{D}_2(I_z = \frac{1}{2} \leftrightarrow \frac{3}{2})$ transition at 3.7 MHz. If there is no laser sweeping, the optical transition connecting the transitions ${}^3\text{H}_4(I_z = \frac{1}{2} \leftrightarrow \frac{3}{2}) \rightarrow {}^1\text{D}_2(I_z = \frac{1}{2} \leftrightarrow \frac{3}{2})$ pumps the ground-state population into the ${}^3\text{H}_4(I_z = \frac{5}{2})$ level, thereby quenching the excited-state ($I_z = \frac{1}{2} \leftrightarrow \frac{3}{2}$) Raman signal.

When the laser is swept to excite the ${}^3\text{H}_4(I_z = \frac{5}{2}) \leftrightarrow {}^1\text{D}_2(I_z = \frac{5}{2})$ transition, the ${}^3\text{H}_4(I_z = \frac{1}{2})$ and ($I_z = \frac{3}{2}$) levels are repopulated, thus providing population to the excited state and a Raman signal is generated. We note that this repopulation is effective only when the opti-

cal transition ${}^3\text{H}_4 I_z = \frac{1}{2}(\frac{3}{2}) \rightarrow {}^1\text{D}_2 I_z = \frac{1}{2}(\frac{3}{2})$ is swept immediately after the transition ${}^3\text{H}_4 I_z = \frac{5}{2} \rightarrow {}^1\text{D}_2 I_z = \frac{5}{2}$. This implies that the Raman signal is generated only when the laser is positively swept (or negatively) but not in the other direction. Whether the signal appears on the positive or negative sweep depends on the absolute ordering of the ground-state hyperfine levels.

We have observed at $H_0 = 0$ G that the ${}^1\text{D}_2(I_z = \frac{1}{2} \leftrightarrow \frac{3}{2})$ resonance is stronger (~ 5 times) when the laser is in a positive sweep, while that of the ${}^1\text{D}_2(I_z = \frac{3}{2} \leftrightarrow \frac{5}{2})$ transition is stronger (~ 5 times) when the laser is in a negative sweep. This observation should allow us to determine the absolute ordering of the ${}^3\text{H}_4$ ground-state hyperfine manifold, thus determining the sign of the quadrupole parameter D . A mathematical model of the optical-pumping cycle as modified by the laser-frequency sweeping is now under investigation.

VI. SENSITIVITY

The ability of the Raman heterodyne technique to detect both cw and pulsed NMR in ground or optically excited state is due to the high sensitivity afforded by the shot-noise-limited performance of the heterodyne process. Here we show a signal-to-noise (S/N) analysis using the cw Raman heterodyne signal of Fig. 4(a).

The total optical power incident on a photodetector is

$$P = P_0(1 + |u|^2 + 2|u| \sin \omega_H t), \quad (6.1)$$

where $P_0 = AcE_0^2/8\pi$ is the input laser power, A and c being the laser-beam cross section and the speed of light, respectively, and $|u| = 2\tilde{E}_s/E_0$ is the AM sideband amplitude Eq. (2.38a). The factor of 2 in $|u|$ is due to the definitions of \tilde{E}_s and E_0 in Eqs. (2.6) and (2.1a). For $|u| \ll 1$, the dc power $P_0 \approx P$ is much greater than either the heterodyne power

$$P_h = 2|u|P_0 \quad (6.2)$$

or the Raman power

$$P_R = |u|^2 P_0 \equiv (P_h/2P_0)^2 P_0. \quad (6.3)$$

The signal in Fig. 4(a) is obtained with an incident power $P_0 = 2.65$ mW, a detection bandwidth $\Delta f = 10$ kHz, signal averaging of $M = 2^{12}$ events, a detection impedance $R = 50 \Omega$, and a photodetector sensitivity $\eta = 0.4$ A/W. Signal averaging improves the signal-to-noise (rms) ratio S/N to a measured value [Fig. 4(a)] of

$$S/N = 110. \quad (6.4)$$

The noise output voltage

$$\bar{v}'_0 = 3.86 \quad (6.5a)$$

[in units of mV(rms)] corresponds to a noise voltage \bar{v}_0 at the detector

$$\bar{v}_0 = \frac{\sqrt{M}}{G} \bar{v}'_0 = 145 \quad (6.5b)$$

[in units of nV(rms)], where $\sqrt{M} = 64$ is the noise reduction due to averaging and $G = 1.7 \times 10^6$ is the gain of the

detection electronics.

The dc photocurrent

$$i = \eta P_0 = 1.06 \quad (6.6)$$

(in units of mA) gives rise to a shot-noise voltage

$$\bar{v}_{\text{SN}} = R \sqrt{2ei\Delta f} = 92 \quad (6.7)$$

in units of nV(rms). At room temperature, the thermal-noise voltage is

$$\bar{v}_{\text{TN}} = \sqrt{4kTR\Delta f} = 91 \quad (6.8)$$

[in units of nV(rms)], which combines with \bar{v}_{SN} to give a total noise voltage of

$$\bar{v}_n = (\bar{v}_{\text{TN}}^2 + \bar{v}_{\text{SN}}^2)^{1/2} = 130 \quad (6.9)$$

[in units of nV(rms)], in agreement with the measured noise $\bar{v}_0 = 145$ nV(rms) [Eq. (6.5b)], thus demonstrating that the technique is shot-noise limited.

The detected heterodyne power Eq. (6.2) is given by

$$P_h = 2|u|P_0 \\ = (S/N)\bar{v}'_0/(GR\eta) = 12.5 \quad (6.10)$$

in units of nW, corresponding to an AM sideband amplitude

$$|u| = P_h/2P_0 = 2.4 \times 10^{-6}.$$

We define the heterodyne power with unity S/N [Eq. (6.10)] as the minimum detectable heterodyne power

$$P_h^{\text{min}} = 1.1 \times 10^{-10}$$

(in units of W), which is equivalent to a minimum detectable Raman power, Eq. (6.3),

$$P_R^{\text{min}} = (P_h^{\text{min}}/2P_0)^2 P_0 \\ = 1.2 \times 10^{-18} \text{ W}, \\ \Leftrightarrow 4 \text{ Raman photons/s}. \quad (6.11)$$

With higher rf and optical powers and a smaller detection bandwidth, this minimum detectable Raman power can easily approach $P_R^{\text{min}} \sim 1 \times 10^{-20}$ W.

In contrast, previous rf-optical techniques^{2,3} which rely on optical hole burning require a substantial change of at least several percent in either fluorescence or transmitted laser power in order to obtain a satisfactory S/N ratio. Here, heterodyne detection enhances the signal in two ways, by (i) detecting the heterodyne power $P_h = 2|u|P_0$ rather than the Raman power $P_R = |u|^2 P_0$, and (ii) allowing detection at a frequency window outside the laser-amplitude noise spectrum, which in our case is from dc to ~ 1 MHz. Furthermore, the technique is not limited by laser-frequency jitter, in first order, or the radiative lifetime of the third level.

VII. SUMMARY AND DISCUSSION

We have described the theory and experimental results of Raman heterodyne detection, a new laser spectroscopic technique for observing NMR. It is shown in theory and

practice that the full range of cw or pulsed NMR can now be explored in either ground or excited electronic states with high precision and sensitivity. We have presented new results on the hyperfine transitions in the $^3\text{H}_4$ ground or $^1\text{D}_2$ excited states of $\text{Pr}^{3+}:\text{LaF}_3$, allowing a comparison with optical dephasing measurements and current or future line-broadening theories. Anomalous line shapes and homogeneous NMR linewidths should stimulate further work in NMR line-broadening theory and in experimental studies in this system and other impurity ion solids.

This technique can be extended in various ways. Its high sensitivity should allow studies of dilute systems in gases and solid state, and of weakly allowed transitions, e.g., in parity-violation experiments.³⁸ In principle, it is applicable to microwave and infrared transitions. The

possibility of nonresonant FM detection makes it more versatile and offers the possibility of generating optical FM sidebands at high frequencies (greater than 1 GHz). It seems clear that this technique has many potential applications.

ACKNOWLEDGMENTS

One of us (N.C.W.) was supported by a Hertz Foundation graduate fellowship and the other (E.S.K.) an IBM graduate fellowship. We acknowledge partial support from the U.S. Office of Naval Research. This work is based in part on the thesis of N. C. Wong, June 1983, in partial fulfillment of the requirements for the Ph.D. degree, Stanford University.

*On leave from the Institut für Quantenoptik, Universität Hannover, D-3000 Hannover, West Germany.

¹J. Mlynek, N. C. Wong, R. G. DeVoe, E. S. Kintzer, and R. G. Brewer, *Phys. Rev. Lett.* **50**, 993 (1983).

²L. E. Erickson, *Opt. Commun.* **21**, 147 (1977).

³R. M. Shelby, C. S. Yannoni, and R. M. Macfarlane, *Phys. Rev. Lett.* **41**, 1739 (1978).

⁴K. Chiang, E. A. Whittaker, and S. R. Hartmann, *Phys. Rev. B* **23**, 6142 (1981).

⁵S. C. Rand, A. Wokaun, R. G. DeVoe, and R. G. Brewer, *Phys. Rev. Lett.* **43**, 1868 (1979); see also R. G. DeVoe, A. Szabo, S. C. Rand, and R. G. Brewer, *ibid.* **42**, 1560 (1979).

⁶R. M. Macfarlane, R. M. Shelby, and R. L. Shoemaker, *Phys. Rev. Lett.* **43**, 1726 (1979).

⁷R. M. Macfarlane, C. S. Yannoni, and R. M. Shelby, *Opt. Commun.* **32**, 101 (1980).

⁸R. G. DeVoe and R. G. Brewer, *Phys. Rev. Lett.* **50**, 1269 (1983).

⁹R. G. DeVoe, A. Wokaun, S. C. Rand, and R. G. Brewer, *Phys. Rev. B* **23**, 3125 (1981), and references therein.

¹⁰R. G. Brewer and R. L. Shoemaker, *Phys. Rev. Lett.* **27**, 631 (1971); R. G. Brewer and A. Z. Genack, *ibid.* **36**, 959 (1976).

¹¹M. D. Levenson, *Introduction to Nonlinear Laser Spectroscopy* (Academic, New York, 1982), p. 17, and references therein.

¹²N. C. Wong, E. S. Kintzer, and R. G. Brewer (unpublished).

¹³J. Mlynek (unpublished).

¹⁴B. S. Mathur, H. Tang, R. Bulos, and W. Happer, *Phys. Rev. Lett.* **21**, 1035 (1968).

¹⁵J. Mlynek, K. H. Drake, G. Kersten, D. Frölich, and W. Lange, *Opt. Lett.* **6**, 87 (1981).

¹⁶R. L. Shoemaker and R. G. Brewer, *Phys. Rev. Lett.* **28**, 1430 (1972); R. G. Brewer and E. L. Hahn, *Phys. Rev. A* **8**, 464 (1973); J. Mlynek and W. Lange, *Opt. Commun.* **30**, 337 (1979).

¹⁷Y. C. Chen, K. Chiang, and S. R. Hartmann, *Phys. Rev. B* **21**, 40 (1980).

¹⁸S. R. Hartmann, *IEEE J. Quantum Electron.* **QE-4**, 802 (1968).

¹⁹P. Hu, S. Geschwind, and T. M. Jedju, *Phys. Rev. Lett.* **37**, 1357 (1976).

²⁰L. E. Erickson, *Phys. Rev. B* **16**, 4731 (1977).

²¹R. G. Brewer, in *Frontiers in Laser Spectroscopy, Proceedings of the Les Houches Summer School, Session XXVII*, edited by R. Balian, S. Haroche, and S. Liberman (North-Holland, Am-

sterdam, 1977), p. 341; L. Allen and J. H. Eberly, *Optical Resonance and Two-Level Atoms* (Wiley-Interscience, New York, 1975).

²²A. G. Redfield, *Phys. Rev.* **98**, 1787 (1955).

²³R. G. Brewer and E. L. Hahn, *Phys. Rev. A* **11**, 1641 (1975); V. P. Chebotayev, in *High Resolution Laser Spectroscopy*, Vol. 13 of *Topics in Applied Physics*, edited by K. Shimoda (Springer, New York, 1976), and references therein; A. Schenzle and R. G. Brewer, *Phys. Rep.* **43**, 455 (1978).

²⁴The last term in Eq. (2.12d) contributes a second-order dc term to ρ_{12} , due to a two-photon transition via level 3, which does not appear in the optical heterodyne signal. The nonresonant term of ρ_{12} that is neglected by the RWA adds a weak, third harmonic term to the heterodyne signal and therefore is not detected.

²⁵*Handbook of Mathematical Functions*, edited by M. Abramowitz and I. A. Stegun (U.S. GPO, Washington, DC, 1972), p. 297; R. G. DeVoe and R. G. Brewer, *Phys. Rev. A* **20**, 2449 (1979).

²⁶Aside from some obvious notational differences, the only definitional change is $\Delta_H = -\omega_{21}$ (as defined in Ref. 1).

²⁷B. R. Reddy and L. E. Erickson, *Phys. Rev. B* **27**, 5217 (1983).

²⁸B. Bleaney, *Physica* **69**, 317 (1973).

²⁹M. A. Teplov, *Zh. Eksp. Teor. Fiz.* **53**, 1510 (1967) [*Sov. Phys.—JETP* **26**, 872 (1968)]; see also A. Wokaun, S. C. Rand, R. G. DeVoe, and R. G. Brewer, *Phys. Rev. B* **23**, 5733 (1981).

³⁰T. P. Das and E. L. Hahn, *Nuclear Quadrupole Resonance Spectroscopy* (Academic, New York, 1958).

³¹R. M. Macfarlane and R. M. Shelby, *Opt. Lett.* **6**, 96 (1981).

³²E. A. Whittaker and S. R. Hartmann, *Phys. Rev. B* **26**, 3617 (1982).

³³A. Abragam, *The Principles of Nuclear Magnetism* (Oxford University Press, London, 1961); C. P. Slichter, *Principles of Magnetic Resonance* (Harper and Row, New York, 1963).

³⁴A. Abragam and K. Kambe, *Phys. Rev.* **91**, 894 (1953).

³⁵R. M. Shelby and R. M. Macfarlane, *Opt. Commun.* **27**, 399 (1978).

³⁶R. M. Macfarlane, D. P. Burum, and R. M. Shelby, *Phys. Rev. Lett.* **49**, 636 (1982).

³⁷R. M. Shelby, R. M. Macfarlane, and C. S. Yannoni, *Phys. Rev. B* **21**, 5004 (1980).

³⁸E. D. Commins and P. H. Bucksbaum, *Annu. Rev. Nucl. Part. Sci.* **30**, 1 (1980).